Simulation characteristics of seismic translation and rotation under the ~~assumption of~~ nonlinearity in small deformation

Wei Li [1,2], Yun Wang [1,2,*], Chang Chen[1,2], Lixia Sun[1,3]

[1] *"MWMC" group, School of Geophysics and Information Technology, China University of Geosciences, Beijing* 100083, *China*

[2] *State Key Laboratory of Geological Processes and Mineral Resources, China University of Geosciences, Beijing* 100083, *China*

[3] *Sinopec Research Institute of Petroleum Engineering Co., Ltd., Beijing* 102206, *China*

[*] Corresponding author: wangyun@mail.gyig.ac.cn.

Abstract Ground motions consist of three translational motions along orthogonal axes and three rotational motions around the axes. Recording all six seismic components facilitates obtaining comprehensive vector wavefield information and restoring complete ground displacement. Classical elastic dynamics of elastic wave propagation assume linearity in small deformations of medium particles. However, seismic rotational observations reveal significant discrepancies between the directly recorded rotational motions in the near field and those derived from calculations based on the traditional theory. Considering that nonlinear effects might be pivotal in contributing to this discrepancy, this study incorporates the previously neglected nonlinearity in small deformation into elastodynamic principles to derive velocity-stress elastic wave equations and apply the staggered-grid finite-difference method to simulate the

propagation of seismic waves. The staggered-grid finite-difference method is then employed to simulate the propagation of seismic waves. Simulations were conducted for the translational and rotational components induced by isotropic (ISO), double couple (DC), and compensated linear vector dipole (CLVD) sources—the three fundamental seismic source types described by moment tensor. These simulations allowed for a comparison of the influence of nonlinearity on wavefield anomalies. The results indicate that the error associated with linear approximation is more pronounced in ISO and CLVD source simulations. The nonlinear effect exhibits a greater impact on rotational motions than translational components, particularly in strong earthquakes. We simulated two actual seismicities Taiwan and compared the synthetic records under linear and nonlinear models. Further explorations are still needed to investigate the specific influence of complex propagation path properties and seismic source mechanisms on nonlinear effects.

~~The conventional theory of elastic-wave propagation is based on classical elastodynamics, assuming linear small deformations of particles. However, recent observations of seismic rotation have revealed significant disparities between actual rotational motions induced by earthquakes in focal areas and near fields compared to theoretical calculations and simulations. Considering the nonlinearity may be the main cause of the discrepancies and based on classical elastodynamic principle, we derive seismic elastic-wave equations with Green strain tensor without the linear small deformation assumption, a different way from using complex nonlinear constitutive relation and try to interpret the mechanism of seismic rotation. By~~

~~simulating and analyzing translational and rotational components subjected to the three basic and typical vibrating sources, namely, isotropic (ISO), double couple (DC), and compensated linear vector dipole (CLVD), represented by moment tensors, we investigate the wavefield differences between elastic wave equations based on linear and nonlinear geometric relations and quantify the differences in homogeneous elastic full-space model. Subsequently, we simulate two observed six-component Taiwan earthquakes and compare their differences caused by nonlinear simulations. The results indicate that linear approximation errors are more pronounced in seismic ISO and CLVD sources. And the nonlinearity of small deformation has a more pronounced effect on rotational motions deduced by strong earthquakes. Also, the nonlinear mechanics of seismic rotation can attribute to the complex propagation paths and source mechanisms simultaneously.~~

1 Introduction

Seismic rotational motions can be ~~are~~ recorded in ground shaking, especially when caused by strong ~~plenty of~~earthquakes~~, especially in~~ (Graiyzer, 1991; ~~Graizer,~~ 2010; Zhou et al., 2019). ~~Several~~ The rotational motions induced by strong earthquakes is particularly prominent in shallow foci and near-field conditions ~~studies have concluded that rotational motions cannot be neglected in shallow foci and near-field seismology~~ (Kozak, 2009; Sun et al., 2017). In the field of architecture engineering, rotation is encouraged to be considered in assessing~~In architecture engineering, rotational torsions are encouraged to be considered in assessing~~ the stability of ground motions and building design ~~design~~ (Li, 1991; Li and Sun, 2001; Yan, 2017; Huras et al., 2021). Several ~~Many~~ studies suggest that incorporating ~~including~~ seismic rotation data, which captures ~~records~~ spatial gradients, ~~will~~ can enhance the precision of earthquake source prediction and moment tensor inversion (Bernauer et al., 2014; Donner, 2016; Ichinose et al., 2021), as supported ~~validated in~~by simulations conducted by Hua and Zhang (2020~~2~~2).

Lee (2007) ~~ever~~ summarized ~~the practical~~ applications of observing seismic rotations ~~i~~on seismic engineering~~n engineering,~~ and inferred that the seismic rotations should mainly contribute to the nonlinear elasticity and site effect, since the real rotational components measured in strong ground motion are greater 1-2 order than the derived ones from translational components. ~~attributing seismic rotation to nonlinear elasticity and site effects. Notably, observed rotations during strong ground motions exceed calculated translational components by one to two orders of~~

~~magnitude.~~ Recognizing the pivotal role of nonlinear waves ~~propagation~~ in addressing geophysical complexities stemming from ~~Earth's~~ Earth's heterogeneities, various analytical solutions of nonlinear wave equations have been ~~advanced~~ developed through iterative techniques ~~based on~~in Green's function (McCall, 1994~~),~~). These ~~including~~ include the flux-corrected transport method (Yang et al., 2002; Zheng et al., 2006)~~,~~ and perturbation approaches (Bataille and Contreras, 2009; Jia et al., 2020) to investigate the nonlinear effects on elastic waves. However, ~~existing~~ most studies primarily focus~~predominantly concentrate~~ on the nonlinear constitutive relations between ~~of~~ stress and strain, ~~traditionally~~ based on small deformation and its linearization assumption~~assuming linear small deformations~~ (Renaud et al., 2012~~;~~ ~~Renaud et al.,;~~ 2013~~b~~; TenCate et al., 2016; Feng et al., 2018~~),~~). There is a scarcity~~ely~~ of ~~exploring~~ exploration into the nonlinearity ~~in geometric relationship~~of deformations, which may represent ~~be~~ a crucial aspect ~~that~~ for ~~could~~ better ~~approximate~~ approximating rotational motions of strong earthquakes ~~rotational motions~~ and near-field ~~seismic~~ conditions.

Taiwan, ~~located~~ situated in an active seismic ~~region~~ zone, broadband seismic observations and studies of physical studies of seismic sources~~where earthquakes have~~ have presented that there are non-ignorable rotational motions in Taiwan's earthquakes and showed different strike-slip rotation characteristics in the south and north of the island~~garnered attention for their special rotational characteristics of distinctive strike-slip, particularly evident in the southern and northern areas, has been highlighted by extensive broadband seismic observations and earthquake-physical~~

102 ~~studies~~ (Yu et al., 1999; Wang and Lv, 2006). Oliveira and Bolt~~'s studies~~ (1989)
103 estimated rotational components of strong motions and verified that the rotation effect
104 could not be neglected in near-field observations on Taiwan Island~~underscore the~~
105 ~~significant impact of rotation in near-field observations on the island,~~. Using
106 measured six-component ground motion data of 52 earthquakes during 2007-2008 at
107 HGSD station in eastern Taiwan, ~~and~~ Chen et al. (2014) pointed out the existence of
108 large vertical rotational motions at near-seismic locations and significant differences
109 in energy and spectral characteristics of horizontal and vertical rotational
110 motions.~~discovered vertical rotations and frequency spectrum variations between~~
111 ~~horizontal and vertical rotations in the near zone of earthquakes from 2007 to 2008.~~
112 These ~~findings~~ studies show ~~incline~~ the importance of seismic rotation~~al~~ ~~studies~~ in
113 ~~unraveling~~ elucidating ~~Taiwan's~~ Taiwan's subsurface ~~underground~~ structures and
114 geodynamics.

115 In this ~~study~~research, we derive the nonlinear wave equations ~~first investigate the~~
116 ~~rotational characteristics~~ and discuss the rotation characteristics under the ~~the~~
117 ~~assumption of~~ nonlinearity in small deformation through numerical simulations of
118 three fundamental ~~basic~~ seismic moment tensor sources. Furthermore~~Additionally~~, we
119 engage in theoretical simulations of six-component (6C) wavefields ~~using~~ of
120 ~~observations from near and strong~~ a near and a strong seismicity~~ies~~ in Taiwan to
121 discuss the effects of nonlinearity~~. We employ the Green strain tensor in the~~
122 ~~simulations of seismic wavefields to discuss the linear approximation and the~~
123 ~~earthquake mechanisms at play in this region~~.

2 Theoryies and method

2.1 Elastodynamic theory

In a three-dimensional orthogonal Cartesian coordinate system, depicting an elastic body within an elastic space, as illustrated in Fig. 1, consider a point A within the elastic body, is denoted as **x**. Point B is adjacent to the point Awhile point B, indicated as **x**+d**x**. The infinitesimal distance separating between A and B is defined as ds. Under Upon instantaneous motivation of an external force, the elastic mass element AB undergoes experiences a displacement $\boldsymbol{u}(\boldsymbol{x}, t)$, transitioning to a new location position A'B'B', . This displacement is accompanied followed by small deformation of the elastic body, where the new positions of A' A' and B' B' are designated as **x**' and **x**'+d**x**', respectively, and with their distance denoted as ds'ds'. The work done by the external force is primarily converted transformed into kinetic energy due todue to the displacement and potential energy stemming from the elastic deformation. Hence, The deformation is quantified by the change in the square of the length of a the line element before and after its deformation is used to measure the deformation, i.e., the squared difference in distance between AB and A'B'A'B', which is mathematically expressed through by Eq. (1). The following equations and tensors are written using the Kronecker symbol and dummy index notation indicator rules.

143

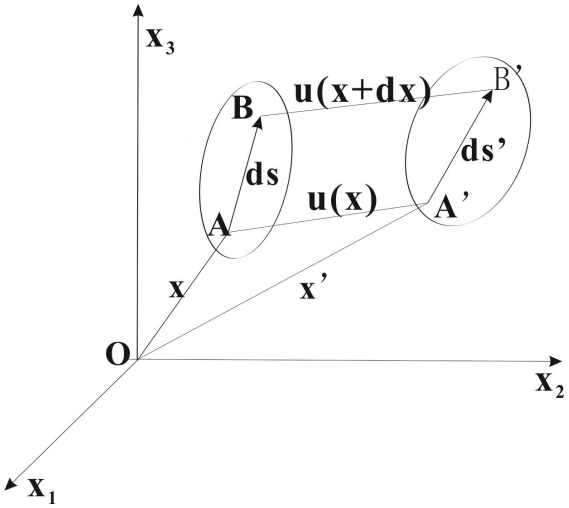

144

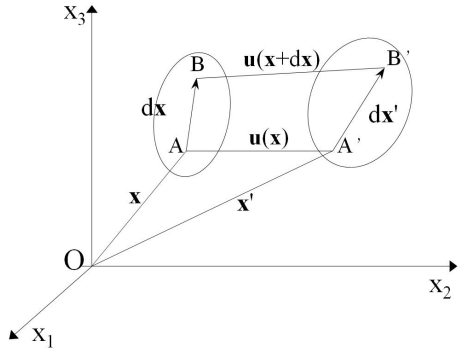

145 **Figure 1.** Schematic diagram of displacement and deformation of an elastomer

146 (Adapted from Aki and Richards (2002))

147 $$(ds')^2-(ds)^2=(\frac{\partial u_j}{\partial x_i}+\frac{\partial u_i}{\partial x_j}+\frac{\partial u_k}{\partial x_i}\cdot\frac{\partial u_k}{\partial x_j})dx_i dx_j,\ i,j\in\{1,2,3\}$~~=x, y, z~~ \quad (1)$$

148 w~~W~~here u_i and u_j ~~denote~~ are the displacements along differen~~t in different~~ directions,

149 and x_i and x_j ~~denote~~ are the ~~specific X, Y, and Z axes in~~ Cartesian coordinates.

150 Therefore, Green strain tensor E_{ij}, given by Eq. (2)~~Eq. (2), known as~~, is an objective

151 measure of deformation ~~of the strain tensor~~ before and after ~~the~~ applying external

152 force to~~deformation of~~ an elastomer.

153 $$E_{ij}=\frac{1}{2}(\frac{\partial u_j}{\partial x_i}+\frac{\partial u_i}{\partial x_j}+\frac{\partial u_k}{\partial x_i}\cdot\frac{\partial u_k}{\partial x_j})$$ –, $i,j\in\{1,2,3\}$ (2)

154 Within the elastodynamic theory, ~~The~~ strain (e_{ij}) and rotation (r_{ij}) tensors ~~in~~

~~elastodynamic theory~~ are defined as follows:

$$e_{ji} = \frac{1}{2}\left(\frac{\partial u_j}{\partial x_i} + \frac{\partial u_i}{\partial x_j}\right) \quad - \quad (3)$$

$$r_{ji} = \frac{1}{2}\left(\frac{\partial u_i}{\partial x_j} - \frac{\partial u_j}{\partial x_i}\right) \quad - \quad (4)$$

~~Then~~Based on Eqs. (3) and (4), the Green strain tensor can also be written as Eq. (5).

$$E_{ij} = e_{ij} + \frac{1}{2}e_{ij}^2 + \frac{1}{2}\left(e_{ij}r_{ij} - r_{ij}e_{ij}\right) - \frac{1}{2}r_{ij}^2 \text{ , } i, j \in \{1,2,3\} \quad (5)$$

The second-order nonlinear displacements in Eq. (2) ~~of nonlinearity in the Green tensor is~~are neglected in the classical elastodynamic theory ~~in the classical theory of kinetic elasticity. ,Instead, it~~ which focuseses ~~solely~~ on the first-order linear terms and neglecting the second-order terms of the strain tensor and the rotation tensor in Eq. (5), thereby ~~simplifying~~ reducing the ~~nonlinear~~ Green strain tensor to its linear approximation e_{ij}.

In isotropic elastic materials, the relationship between strain and stress used to characterize an elastomer is:

$$\sigma_{ij} = \lambda\delta_{ij}e_{kk} + 2\mu e_{ij} \text{ , } i, j \in \{1,2,3\} \quad (6)$$

where λ and μ are Lamé coefficients, and δ is the Kronecker symbol. Normally, the equation uses the conventional linear approximation e_{ij}, and the principal strains: $\theta = \partial u_1/x_1 + \partial u_2/x_2 + \partial u_3/x_3 = e_{11} + e_{22} + e_{33}$. Include the nonlinearity during elastomer's deformation by using the strain tensor E_{ij} and the principal strains $\theta_E = E_{11} + E_{22} + E_{33}$ in Eq. (6). The Eq. (6) can be simply written as Eq. (7).

$$\sigma_{ij} = \lambda\delta_{ij}E_{kk} + 2\mu E_{ij} \text{ , } i, j \in \{1,2,3\} \quad (7)$$

$\rho \frac{\partial^2 u_i}{\partial t^2} = \frac{\partial \sigma_{ji}}{\partial x_j}$ Then, substituting Eq. (7) containing nonlinear contributions into Eq. (8) representing the stress-strain relationship yields Eq. (9), where ρ is the material density.

$$\rho \frac{\partial^2 u_i}{\partial t^2} = \frac{\partial \sigma_{ji}}{\partial x_j}, \; i, j \in \{1,2,3\} \tag{8}$$

$$\rho \frac{\partial^2 u_i}{\partial t^2} = \frac{\partial}{\partial x_j}\left(\lambda E_{kk}\delta_{ij} + 2\mu E_{ij}\right) = (\lambda+\mu)\frac{\partial \theta}{\partial x_i} + \mu \frac{\partial^2 u_i}{\partial x_j \partial x_j} + \lambda \delta_{ij} \frac{\partial^2 u_k}{\partial x_i x_j} \cdot \frac{\partial u_k}{\partial x_j} + \mu \left(\frac{\partial^2 u_k}{\partial x_i x_j} \cdot \frac{\partial u_k}{\partial x_j} + \frac{\partial^2 u_k}{\partial x_j x_j} \cdot \frac{\partial u_k}{\partial x_i} \right),$$

$$i, j \in \{1,2,3\} \tag{9}$$

In Eq. (9), the first two terms on the right side of the equal sign are the results of the wave equation under the linear strain tensor, and the last two terms are the increased terms in the wave equation after the nonlinear strain is applied. Eq. (9) shows the difference in equation expression between using the linear and nonlinear strains.

Compared to the original equation which contains only the first two terms of the right of the equal sign in Eq. (9). The nonlinearity introduces several third-order terms that add more physical complexity via material's elastic property. The part associated with the bulk modulus λ reflects that the volumetric deformation is no longer limited to the original purely linear principal strains but also the volumetric change induced by shear deformation, which is an important feature of the material's nonlinear elastic behavior. The part related to the shear modulus μ additionally describes the shear deformation property. The elastic shear deformation is not merely a direct consequence of shear stress but also exhibits a correlation with the principal strains shown in Eq. (9). The additional terms in Eq. (9) do not directly correspond to the

wavefield difference, and in earthquakes, their manifestation may vary depending on the material properties and source loading. Therefore, it is necessary to assess the effect of the material's nonlinear elasticity on seismic wave propagation by specific theoretical numerical simulations.~~Eq. (10) exhibits more complexity, signifying the introduction of additional physical intricacies into an elastomer's deformation dynamics. The nonlinearity associated with the shear modulus μ engenders nonlinear effects through the strain tensor, while the increment associated with the bulk modulus λ induces nonlinear effects through the volumetric strain.The disparity between the two wave equationsdoes not directly translate to the final displacement field discrepancies. The displacement field in Eq. (10) is the result of the nonlinear small deformation, in contrast to Eq. (9), where such nonlinear effects are absent. Therefore, the velocity-stress equations using the Green strain tensor are derived next to compare the difference in wave fields between the two by numerical simulation of seismic wavefields.~~

2.2 Staggered-grid finite-difference simulation method~~Velocity-stress elastic wave equations~~

The staggered-grid finite-difference method has been ~~is well-established~~ a technique for ~~performing~~ numerical simulations of seismic wavefields. In this method, the medium is divided into two grid systems and velocity-stress wave equations are discretized in these grids, thereby allowing computing the~~By discretizing the medium and the wave equations, the~~ numerical solution of ~~the~~ wavefield~~s is obtained~~ at

each grid point ~~under each time node~~ as time ~~time~~ progresses (Madariaga, 1976; Sun et al., 2018). For example, the grid configuration for a two-dimensional scenario is shown in Fig. 2.

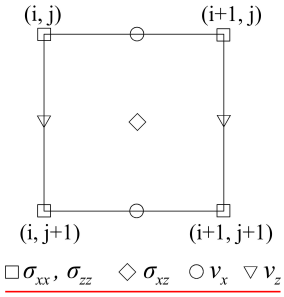

Figure 2. Schematic diagram of 2D staggered grids

Similar to the process of obtaining the velocity-stress equations in three-dimensional (3D) elastic isotropic media using conventional linear strain (Pei, 2005). Firstly, the individual stress components using the nonlinear strain **E** are givern in Eq. (10).~~the first-order velocity-stress wave equations~~

$$
\begin{aligned}
\sigma_{xx} &= \lambda\left\{\frac{\partial u_x}{\partial x}+\frac{\partial u_y}{\partial y}+\frac{\partial u_z}{\partial z}+\frac{1}{2}\left[\left(\frac{\partial u_x}{\partial x}\right)^2+\left(\frac{\partial u_y}{\partial x}\right)^2+\left(\frac{\partial u_z}{\partial x}\right)^2+\left(\frac{\partial u_x}{\partial y}\right)^2+\left(\frac{\partial u_y}{\partial y}\right)^2+\left(\frac{\partial u_z}{\partial y}\right)^2+\left(\frac{\partial u_x}{\partial z}\right)^2+\left(\frac{\partial u_y}{\partial z}\right)^2+\left(\frac{\partial u_z}{\partial z}\right)^2\right]\right\}+\mu\left[\frac{\partial u_x}{\partial x}+\left(\frac{\partial u_x}{\partial x}\right)^2+\left(\frac{\partial u_y}{\partial x}\right)^2+\left(\frac{\partial u_z}{\partial x}\right)^2\right]\\
\sigma_{yy} &= \lambda\left\{\frac{\partial u_x}{\partial x}+\frac{\partial u_y}{\partial y}+\frac{\partial u_z}{\partial z}+\frac{1}{2}\left[\left(\frac{\partial u_x}{\partial x}\right)^2+\left(\frac{\partial u_y}{\partial x}\right)^2+\left(\frac{\partial u_z}{\partial x}\right)^2+\left(\frac{\partial u_x}{\partial y}\right)^2+\left(\frac{\partial u_y}{\partial y}\right)^2+\left(\frac{\partial u_z}{\partial y}\right)^2+\left(\frac{\partial u_x}{\partial z}\right)^2+\left(\frac{\partial u_y}{\partial z}\right)^2+\left(\frac{\partial u_z}{\partial z}\right)^2\right]\right\}+\mu\left[\frac{\partial u_y}{\partial y}+\left(\frac{\partial u_x}{\partial y}\right)^2+\left(\frac{\partial u_y}{\partial y}\right)^2+\left(\frac{\partial u_z}{\partial y}\right)^2\right]\\
\sigma_{zz} &= \lambda\left\{\frac{\partial u_x}{\partial x}+\frac{\partial u_y}{\partial y}+\frac{\partial u_z}{\partial z}+\frac{1}{2}\left[\left(\frac{\partial u_x}{\partial x}\right)^2+\left(\frac{\partial u_y}{\partial x}\right)^2+\left(\frac{\partial u_z}{\partial x}\right)^2+\left(\frac{\partial u_x}{\partial y}\right)^2+\left(\frac{\partial u_y}{\partial y}\right)^2+\left(\frac{\partial u_z}{\partial y}\right)^2+\left(\frac{\partial u_x}{\partial z}\right)^2+\left(\frac{\partial u_y}{\partial z}\right)^2+\left(\frac{\partial u_z}{\partial z}\right)^2\right]\right\}+\mu\left[\frac{\partial u_x}{\partial z}+\left(\frac{\partial u_x}{\partial z}\right)^2+\left(\frac{\partial u_y}{\partial z}\right)^2+\left(\frac{\partial u_z}{\partial z}\right)^2\right]\\
\sigma_{xy} &= \sigma_{yx} = \mu\left(\frac{\partial u_x}{\partial y}+\frac{\partial u_y}{\partial x}+\frac{\partial u_x}{\partial x}\frac{\partial u_x}{\partial y}+\frac{\partial u_y}{\partial x}\frac{\partial u_y}{\partial y}+\frac{\partial u_z}{\partial x}\frac{\partial u_z}{\partial y}\right)\\
\sigma_{zy} &= \sigma_{yz} = \mu\left(\frac{\partial u_y}{\partial z}+\frac{\partial u_z}{\partial y}+\frac{\partial u_x}{\partial z}\frac{\partial u_x}{\partial y}+\frac{\partial u_y}{\partial z}\frac{\partial u_y}{\partial y}+\frac{\partial u_z}{\partial z}\frac{\partial u_z}{\partial y}\right)\\
\sigma_{xz} &= \sigma_{zx} = \mu\left(\frac{\partial u_x}{\partial z}+\frac{\partial u_z}{\partial x}+\frac{\partial u_x}{\partial x}\frac{\partial u_x}{\partial z}+\frac{\partial u_y}{\partial x}\frac{\partial u_y}{\partial z}+\frac{\partial u_z}{\partial x}\frac{\partial u_z}{\partial z}\right)
\end{aligned}
\tag{10}
$$

~~Where σ_{ji} denotes the stress tensor, v_x, v_y, and v_z denote the velocity of X, Y, and Z components. R_{xz} corresponds to the rotation rate around Y axis, commonly referred to as RY in rotational seismology, as well as R_X and R_Z.~~

Then, a first-order partial derivative with respect to time is taken on both sides of

Eq. (10), with Eq. (8), and the displacement is converted to velocity term, the velocity-stress equations of nonlinear elasticity used for finite-difference method are obtained in Eq. (11):~~Similarly, the velocity-stress elastic wave equations under the assumption of nonlinear small deformation in 3D isotropic media can be given as Eq. (12).~~

$$
\begin{cases}
\dfrac{\partial \sigma_{xx}}{\partial x}+\dfrac{\partial \sigma_{yx}}{\partial y}+\dfrac{\partial \sigma_{zx}}{\partial z}=\rho\dfrac{\partial v_x}{\partial t} \\
\dfrac{\partial \sigma_{yx}}{\partial x}+\dfrac{\partial \sigma_{yy}}{\partial y}+\dfrac{\partial \sigma_{yz}}{\partial z}=\rho\dfrac{\partial v_y}{\partial t} \\
\dfrac{\partial \sigma_{zx}}{\partial x}+\dfrac{\partial \sigma_{zy}}{\partial y}+\dfrac{\partial \sigma_{zz}}{\partial z}=\rho\dfrac{\partial v_z}{\partial t}
\end{cases}
$$

$$
\begin{cases}
\dfrac{\partial \sigma_{xx}}{\partial t}=(\lambda+2\mu)\dfrac{\partial v_x}{\partial x}+\lambda\dfrac{\partial v_y}{\partial y}+\lambda\dfrac{\partial v_z}{\partial z}+dt\cdot(\lambda+2\mu)\cdot(\dfrac{\partial v_x}{\partial x}\dfrac{\partial v_x}{\partial x}+\dfrac{\partial v_y}{\partial x}\dfrac{\partial v_y}{\partial x}+\dfrac{\partial v_z}{\partial x}\dfrac{\partial v_z}{\partial x})+dt\cdot\lambda\cdot(\dfrac{\partial v_x}{\partial y}\dfrac{\partial v_x}{\partial y}+\dfrac{\partial v_y}{\partial y}\dfrac{\partial v_y}{\partial y}+\dfrac{\partial v_z}{\partial y}\dfrac{\partial v_z}{\partial y})+dt\cdot\lambda\cdot(\dfrac{\partial v_x}{\partial z}\dfrac{\partial v_x}{\partial z}+\dfrac{\partial v_y}{\partial z}\dfrac{\partial v_y}{\partial z}+\dfrac{\partial v_z}{\partial z}\dfrac{\partial v_z}{\partial z}) \\
\dfrac{\partial \sigma_{yy}}{\partial t}=\lambda\dfrac{\partial v_x}{\partial x}+(\lambda+2\mu)\dfrac{\partial v_y}{\partial y}+\lambda\dfrac{\partial v_z}{\partial z}+dt\cdot\lambda\cdot(\dfrac{\partial v_x}{\partial x}\dfrac{\partial v_x}{\partial x}+\dfrac{\partial v_y}{\partial x}\dfrac{\partial v_y}{\partial x}+\dfrac{\partial v_z}{\partial x}\dfrac{\partial v_z}{\partial x})+dt\cdot(\lambda+2\mu)\cdot(\dfrac{\partial v_x}{\partial y}\dfrac{\partial v_x}{\partial y}+\dfrac{\partial v_y}{\partial y}\dfrac{\partial v_y}{\partial y}+\dfrac{\partial v_z}{\partial y}\dfrac{\partial v_z}{\partial y})+dt\cdot\lambda\cdot(\dfrac{\partial v_x}{\partial z}\dfrac{\partial v_x}{\partial z}+\dfrac{\partial v_y}{\partial z}\dfrac{\partial v_y}{\partial z}+\dfrac{\partial v_z}{\partial z}\dfrac{\partial v_z}{\partial z}) \\
\dfrac{\partial \sigma_{zz}}{\partial t}=\lambda\dfrac{\partial v_x}{\partial x}+\lambda\dfrac{\partial v_y}{\partial y}+(\lambda+2\mu)\dfrac{\partial v_z}{\partial z}+dt\cdot\lambda\cdot(\dfrac{\partial v_x}{\partial x}\dfrac{\partial v_x}{\partial x}+\dfrac{\partial v_y}{\partial x}\dfrac{\partial v_y}{\partial x}+\dfrac{\partial v_z}{\partial x}\dfrac{\partial v_z}{\partial x})+dt\cdot\lambda\cdot(\dfrac{\partial v_x}{\partial y}\dfrac{\partial v_x}{\partial y}+\dfrac{\partial v_y}{\partial y}\dfrac{\partial v_y}{\partial y}+\dfrac{\partial v_z}{\partial y}\dfrac{\partial v_z}{\partial y})+dt\cdot(\lambda+2\mu)\cdot(\dfrac{\partial v_x}{\partial z}\dfrac{\partial v_x}{\partial z}+\dfrac{\partial v_y}{\partial z}\dfrac{\partial v_y}{\partial z}+\dfrac{\partial v_z}{\partial z}\dfrac{\partial v_z}{\partial z}) \\
\dfrac{\partial \sigma_{xy}}{\partial t}=\mu(\dfrac{\partial v_y}{\partial x}+\dfrac{\partial v_x}{\partial y})+dt\cdot 2\mu\cdot(\dfrac{\partial v_x}{\partial x}\dfrac{\partial v_x}{\partial y}+\dfrac{\partial v_y}{\partial x}\dfrac{\partial v_y}{\partial y}+\dfrac{\partial v_z}{\partial x}\dfrac{\partial v_z}{\partial y}) \\
\dfrac{\partial \sigma_{xz}}{\partial t}=\mu(\dfrac{\partial v_x}{\partial z}+\dfrac{\partial v_z}{\partial x})+dt\cdot 2\mu\cdot(\dfrac{\partial v_x}{\partial z}\dfrac{\partial v_x}{\partial x}+\dfrac{\partial v_y}{\partial z}\dfrac{\partial v_y}{\partial x}+\dfrac{\partial v_z}{\partial z}\dfrac{\partial v_z}{\partial x}) \\
\dfrac{\partial \sigma_{yz}}{\partial t}=\mu(\dfrac{\partial v_z}{\partial y}+\dfrac{\partial v_y}{\partial z})+dt\cdot 2\mu\cdot(\dfrac{\partial v_x}{\partial y}\dfrac{\partial v_x}{\partial z}+\dfrac{\partial v_y}{\partial y}\dfrac{\partial v_y}{\partial z}+\dfrac{\partial v_z}{\partial y}\dfrac{\partial v_z}{\partial z})
\end{cases}
\tag{11}
$$

where v_i ($i\in\{x,y,z\}$) is the velocity component along the Cartesian coordinate, and dt is the time interval. In addition, the rotation rates around the Cartesian Coordinate axes are:

$$
\begin{cases}
R_x=\dfrac{1}{2}(\dfrac{\partial v_z}{\partial y}-\dfrac{\partial v_y}{\partial z}) \\
R_y=\dfrac{1}{2}(\dfrac{\partial v_x}{\partial z}-\dfrac{\partial v_z}{\partial x}) \\
R_z=\dfrac{1}{2}(\dfrac{\partial v_y}{\partial x}-\dfrac{\partial v_x}{\partial y})
\end{cases}
\tag{12}
$$

~~Where the variables and symbols are defined in the same way as in Eq. (11).~~

Based on the linear and nonlinear velocity-stress equations Eqs. (11) and (12), We wrote C/C++ language code to numerically simulate the propagation of seismic

waves. To weaken boundary reflections, perfectly matched absorbing layer boundary conditions are adapted to the boundaries (Dong and Ma 2000). And acoustic boundary replacement method (shown in Eq. (13)) is employed to ensure the application of free-surface at upper boundary, which defines the free-surface condition at corresponding z-axis position (Xu et al., 2007; Wang et al., 2012)

$$\begin{cases} \sigma_{zz} = 0 \\ \rho = 0.5\rho_0 \\ \lambda = 0 \\ 2\mu = \mu_0 \end{cases} \tag{13}$$

where σ_{zz}, ρ, λ, and μ represent the normal stress, medium density, and Lamé coefficients at and above the free surface, respectively. ρ_0 and μ_0 represent the medium density and Lamé coefficients below the free surface, respectively.

3 ~~Wavefield~~ Ssimulations of ~~three types of~~ basic seismic moment sources

3.1 Forward modelling parameters

In the physical process of seismic sources, when the seismic wavelength of interest exceeds the scale of involved source, the source can be regarded as a point source. The seismic moment tensor, as represented in Eq. (14), is the most comprehensive depiction of the seismic point source (Gilbert, 1971).

$$\boldsymbol{M} = \begin{pmatrix} M_{xx} & M_{xy} & M_{xz} \\ M_{yx} & M_{yy} & M_{yz} \\ M_{zx} & M_{zy} & M_{zz} \end{pmatrix} \tag{14}$$

The moment tensor **M** is a symmetric second-order matrix, with each element representing a moment component acting in corresponding direction. It describes the distribution of stress at epicenter and is a crucial parameter for understanding the

properties of seismic radiation fields. The moment tensor can be decomposed into three distinct components: isotropy component (ISO), double couple component (DC), and compensated linear vector dipole component (CLVD) (Knopoff and Randall, 1970; Jost and Hermann, 1989). Specifically, the ISO component represents the volume change of focal area, and its moment tensor is characterized by a non-zero trace and uniform force in three principal axes. The DC component signifies the dislocation of two walls of earthquake-induced fault without any volume variation. The moment tensor of the CLVD component consists of three vector dipoles as ISO, characterized by one dipole being twice as large as the other two. The expressions for these three basic seismic source components can be written as shown below. Understanding the wavefield characteristics of these three representative basic seismic sources is important to understanding seismic radiation and the propagation of seismic waves.

$$\boldsymbol{M}^{ISO} = \begin{pmatrix} M_{xx} & 0 & 0 \\ 0 & M_{yy} & 0 \\ 0 & 0 & M_{zz} \end{pmatrix} \tag{15}$$

$$\boldsymbol{M}^{DC} = \begin{pmatrix} 0 & M_{xy} & 0 \\ M_{yx} & 0 & 0 \\ 0 & 0 & 0 \end{pmatrix} \tag{16}$$

$$\boldsymbol{M}^{CLVD} = \begin{pmatrix} M_{xx} & 0 & 0 \\ 0 & M_{yy} & 0 \\ 0 & 0 & -2M_{zz} \end{pmatrix} \tag{17}$$

According to the implementation of seismic moment sources in finite-difference method Graves (1996), the body force represented by the moment tensor can be converted into a velocity source by adding it to velocity components. The specific

loading equations for the three moment sources in the grid system are Eqs. (18), (19), and (20).

$$\text{ISO}: \begin{cases} \Delta v_x^{n+\frac{1}{2}}\left(i+\frac{1}{2},j,k\right)=\frac{M_{xx}dt}{\rho Vdx}f^n \\ \Delta v_x^{n+\frac{1}{2}}\left(i-\frac{1}{2},j,k\right)=\frac{-M_{xx}dt}{\rho Vdx}f^n \\ \Delta v_y^{n+\frac{1}{2}}\left(i,j+\frac{1}{2},k\right)=\frac{M_{yy}dt}{\rho Vdy}f^n \\ \Delta v_y^{n+\frac{1}{2}}\left(i,j-\frac{1}{2},k\right)=\frac{-M_{yy}dt}{\rho Vdy}f^n \\ \Delta v_z^{n+\frac{1}{2}}\left(i,j,k+\frac{1}{2}\right)=\frac{M_{zz}dt}{\rho Vdz}f^n \\ \Delta v_z^{n+\frac{1}{2}}\left(i,j,k-\frac{1}{2}\right)=\frac{-M_{zz}dt}{\rho Vdz}f^n \end{cases} \quad (17\,18)$$

$$\text{DC}: \begin{cases} \Delta v_x^{n+\frac{1}{2}}\left(i+\frac{1}{2},j,k\right)=\frac{-M_{xy}dt}{\rho Vdy}f^n \\ \Delta v_x^{n+\frac{1}{2}}\left(i+\frac{1}{2},j-1,k\right)=\frac{M_{xy}dt}{\rho Vdy}f^n \\ \Delta v_y^{n+\frac{1}{2}}\left(i,j-\frac{1}{2},k\right)=\frac{M_{yx}dt}{\rho Vdx}f^n \\ \Delta v_y^{n+\frac{1}{2}}\left(i+1,j-\frac{1}{2},k\right)=\frac{-M_{yx}dt}{\rho Vdx}f^n \end{cases} \quad (19)$$

$$\text{CLVD}: \begin{cases} \Delta v_x^{n+\frac{1}{2}}\left(i+\frac{1}{2},j,k\right)=\frac{M_{xx}dt}{\rho Vdx}f^n \\ \Delta v_x^{n+\frac{1}{2}}\left(i-\frac{1}{2},j,k\right)=\frac{-M_{xx}dt}{\rho Vdx}f^n \\ \Delta v_y^{n+\frac{1}{2}}\left(i,j+\frac{1}{2},k\right)=\frac{M_{yy}dt}{\rho Vdy}f^n \\ \Delta v_y^{n+\frac{1}{2}}\left(i,j-\frac{1}{2},k\right)=\frac{-M_{yy}dt}{\rho Vdy}f^n \\ \Delta v_z^{n+\frac{1}{2}}\left(i,j,k+\frac{1}{2}\right)=\frac{-2M_{zz}dt}{\rho Vdz}f^n \\ \Delta v_z^{n+\frac{1}{2}}\left(i,j,k-\frac{1}{2}\right)=\frac{2M_{zz}dt}{\rho Vdz}f^n \end{cases} \quad (20)$$

where Δv is the velocity increment, n and dt are the time node and interval, and ρ and V are the medium density and the unit volume of the model. The source-time function f^n corresponds to the amplitude of wavelet at the ndt moment.

In the numerical simulations, the Ricker wavelet with a dominant frequency of 0.5 Hz was utilized as the source wavelet. In order to focus on the influence of nonlinearity on seismic waves generated by different types of moment sources, we currently only discuss the simulations in a 3D homogeneous isotropic full-space model. The model size is 80 km (x) × 80 km (y)× 80 km (z), with 0.5-km grid

division in three directions. The medium physical properties are v_p=4400 m/s, v_s=3000 m/s, ρ=2600 kg/m^3. The epicenter is located at the center of the model (40km, 40 km, 40 km). The time sampling interval is 15 ms, and the total recording time spans 9 seconds, using second-order time and sixth-order spatial difference approximation.

~~3.1~~3.2 Results ~~ISO source~~

3.2.1 ISO source

Under the ~~assumption of nonlinear~~wave equations containing nonlinearity in small deformation ~~related to the condition of the Green strain tensor~~, Fig. 3a displays 8th second 6C wavefield snapshots induced by the ISO source, revealing consistent P-wave amplitudes in translational components but near absence in rotational components.

~~the 3-component translational and rotational seismic snapshots are synthesized and illustrated in Fig. 3a. These snapshots demonstrate the generation of solely P-wave, with minimal energy projected in rotational components upon the excitation of ISO source.~~

Fig. 3b highlights wavefield differences between linear and nonlinear conditions, showing that P waves persist in translational components but are very weak in rotation, where S-waves unexpectedly emerge~~To highlight the distinction in wave propagation between linear and nonlinear conditions, we present the wavefield difference and their approximation with the relative change in Fig. 3b and c.~~. ISO sources generate P waves, and in linear theory, since the volume change of elastic material is solely

associated with a pure pressure field of compression or expansion. So, only P-waves propagate in homogeneous and isotropic media. However, Fig. 3b demonstrates unique nonlinear media characteristics, enabling P-S wave coupling and energy conversion. This occurs due to nonlinear volumetric strain terms related to shear strains, disrupting linear theory's independent P-S wave propagation constraint.~~Minimal disparities are observed in P-wave fronts, indicating that the assumption of linear small deformation is satisfied for P-wave in ISO source simulation. Conversely, examining the S-wave fronts in Fig. 3b and their relative changes (ranging approximately between 5-20 percent) in Fig. 3c lead to the conclusion that even in the ISO simulation, the coupling of P- and S-waves in the wave equations allows the generation of S-waves, a phenomenon that is unattainable under conditions of linear small deformation.~~

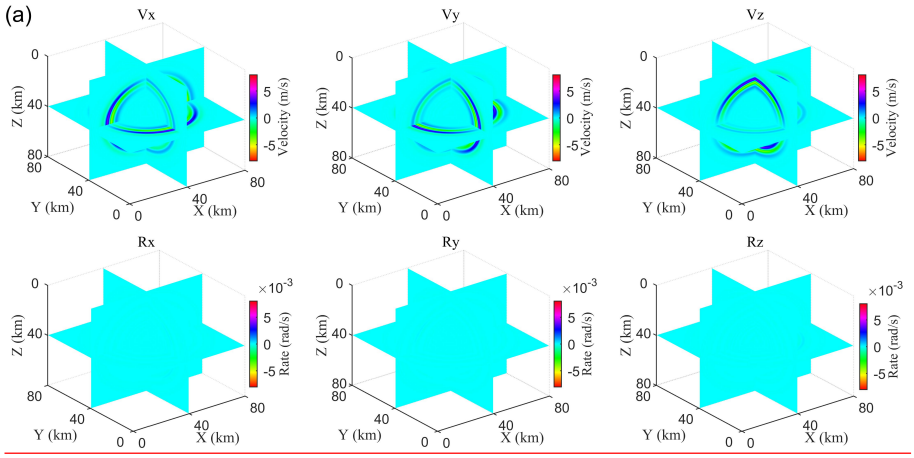

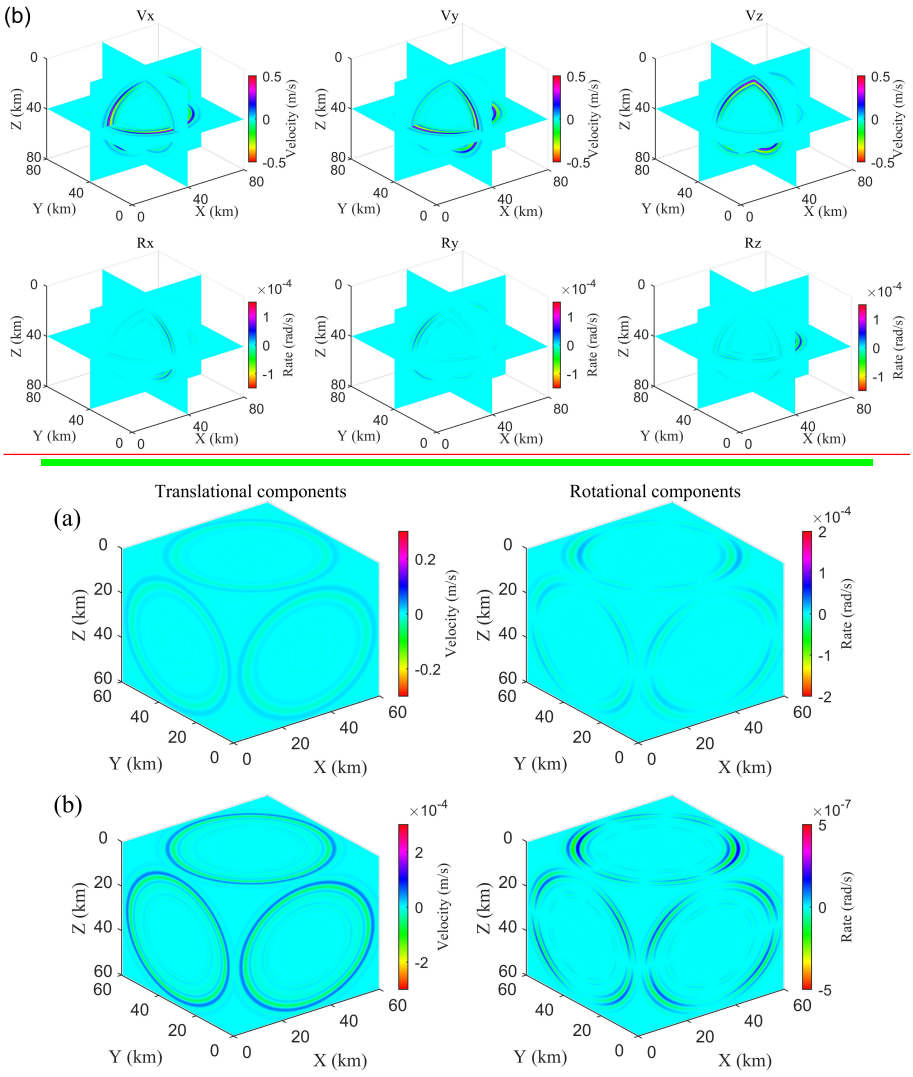

Figure 3. Snapshots of (a) 6C ~~Wavefield~~ wavefield ~~comparisons at 8th second excited by ISO source~~in nonlinear model and (b) wavefield difference between linear and nonlinear models at 8th second excited by ISO source (Mw7)

~~. (a) presents the wavefield snapshots under nonlinear small deformation, (b) presents the difference between linear and nonlinear conditions, and (c) presents their relative change in percentage (using the linear result as the denominator)~~

~~3.2 DC source~~

3.2.2 DC source

The wavefields excited by the DC source in the nonlinear model are illustrated in Fig. 4a~~, revealing the generation of relatively weak P and stronger S waves. The application of double force moments (M_{xy} and M_{yx}) loaded within the x-y plane results in the X- and Y-components of translational motions being stronger than the Z-component. Consequently, the $\mathbf{R}_Z$ exhibits a greater degree of wavefield energy than the $\mathbf{R}_X$ and $\mathbf{R}_Y$ components. From the wavefield differences and relative change between the two assumptions (Fig. 4b and c), it becomes evident that the discrepancy in S-wave is notable, and the relative change in P wave is more prominent in the rotational components (below 10 %). Moreover, the distinction in the wavefront polarity of the P- and S-wave in the wavefield caused by nonlinearity is totally different from the polarity of the wavefield itself, as illustrated in Fig. 4a~~. The DC source primarily generates S-waves with higher energy, with P-waves being comparatively weaker. The loaded force couple, Mxy and Myx, enhances the waves in the Vx and Vy components relative to the Vz component. Similarly, the Rz-component waves are more pronounced than in the Rx and Ry components. Wavefield difference in Fig. 4b shows nearly one order of magnitude difference in intensity between the difference wavefields and the original wavefields. P- and S-wave intensities are nearly equal in translational components, while S-waves dominate in Rx and Ry components.

In addition, Fig. 4b reveals distinct wavefront polarities for P and S waves influenced by nonlinear terms, differing from those in Fig. 4a. This indicates that nonlinear effects on seismic waves from DC-type source may differ from those of

ISO-type source. That is, nonlinearity's impact on seismic waves from shear force sources contrasts with pressure sources, potentially being more complex and leading to the deviations of polarity of wavefield from the original wavefield.

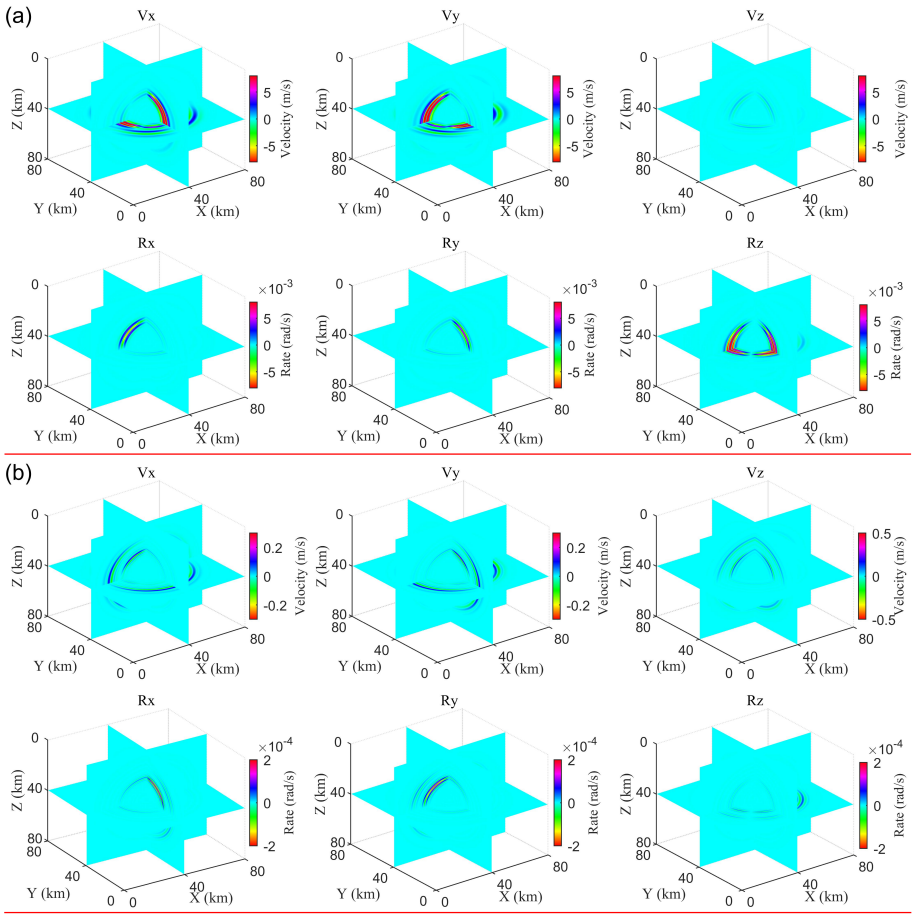

Figure 4. Snapshots of (a) 6C wavefield in nonlinear model and (b) wavefield difference between linear and nonlinear models at 8th second excited by DC source (Mw7)~~Wavefield comparisons at 8th second excited by DC source. (a) presents the wavefield snapshots under nonlinear small deformation, (b) presents the difference between the linear and nonlinear conditions, and (c) presents their relative change with percentage (using the linear result as the denominator)~~

~~3.3 CLVD source~~

3.2.3 CLVD source

Fig. 5a displays the results ~~generated~~ for ~~by~~ the CLVD source simulation. ~~I~~ The intensities of P- and S-waves are approximately equal in the translational components, whereas in the rotational components, S-waves dominate with the Rz component being notably weaker. The wavefield discrepancies shown in Fig. 5b emphasize the significant intensity of S-wave discrepancies in the rotational components, underscoring their superiority in capturing S-waves propagating through nonlinear media.

It is evident that the polarity of wavefield discrepancies due to nonlinearity in the CLVD source simulation aligns with that observed in the DC source simulation (Fig. 4b). The results may suggest that since both CLVD and DC-type force sources generate seismic waves in a non-volumetric manner, nonlinearity leads to particularly prominent volume changes due to shear stresses. This similarity may arise from their shared force characteristics of the seismic sources, resulting in comparable nonlinear response characteristics.~~n comparison to the outcomes of ISO and DC sources, the CLVD elicits more pronounced S waves primarily projected in $\mathbf{R}_X$ and $\mathbf{R}_Y$ components. Moreover, the wavefield differences between linearity and nonlinearity intensify, particularly in S wave in rotational motion (Fig. 5b). Their maximum relative change can reach up to 10 percent, especially along the diagonal direction of 45 degrees (Fig. 5c).~~

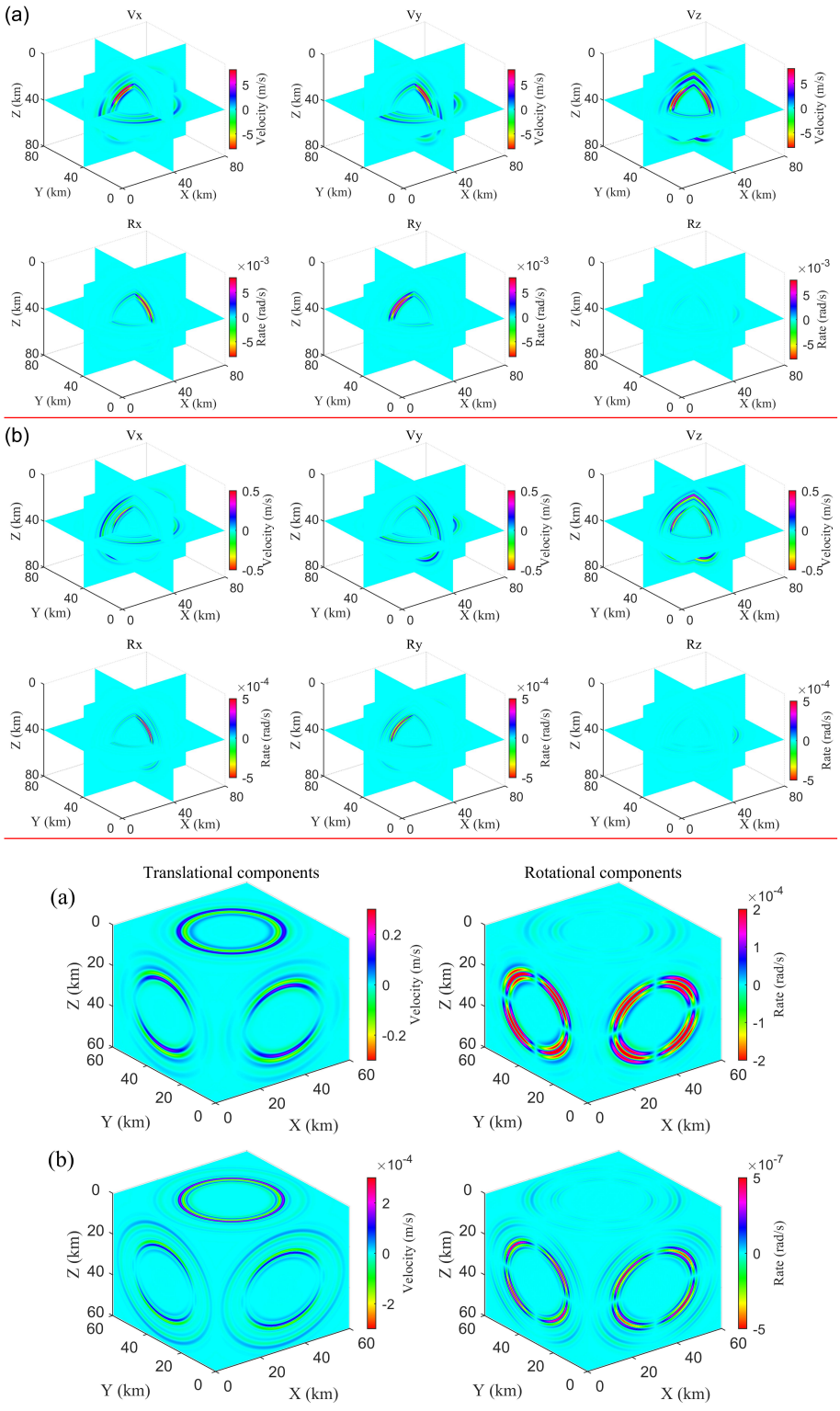

Figure 5. Snapshots of (a) 6C wavefield in nonlinear model and (b) wavefield difference between linear and nonlinear models at 8th second excited by CLVD source (Mw7)~~**Figure 5.** Wavefield comparisons at 8th second excited by CLVD source. (a) presents the wavefield snapshots under nonlinear small deformation, (b)~~

~~presents the difference between the linear and nonlinear conditions, and (c) presents their relative change with percentage (using the linear result as the denominator)~~

3.~~4~~ 3 Wavefield c~~C~~omparisons ~~of wavefield energy for basic seismic sources~~

The comparison highlights disparities in wavefields of nonlinear elastic waves across both translational and rotational components. We synthesized the seismic wavefield for moment magnitudes ranging from 2 to 7 and analyzed wavefield energy E variations at 6th second of propagation for the three source simulations in both nonlinear and linear models (Fig. 6). The wavefield energy was approximated using Eq. (21):

$$E = \sum_{i,j,k} v_{i,j,k}^2 \Delta V \tag{21}$$

where $v_{i,j,k}$ is the wavefield value at each grid, and ΔV is the unit grid volume.

Fig. 6 displays variations in nonlinear effects across moment magnitudes. The ISO source (Fig. 6a) exhibits a more significant relative error in the wavefield compared to the CLVD source (Fig. 6b), while the DC source (Fig. 6c) yields the most minor relative error among the three models. Across these sources, the wavefield energy change rate increases exponentially with magnitude. At magnitude 7, the rate reaches 10% for the ISO source and 5% for the CLVD source. For magnitudes below 4, nonlinear effects are minimal. However, in moderate-to-large earthquakes (magnitudes > 4), the relative alteration in the rotational components becomes more substantial than in the translational components. Given that the DC source typically dominates focal mechanisms for most earthquakes (Zhao and Zhang, 2022), we infer

that the linear approximation suffices for modeling most earthquakes (solely involving body waves). However, this approximation may break down in intense seismic activity, particularly when considering rotational components.

~~The disparities in propagation of nonlinear elastic waves in homogeneous media are predominantly observed in rotational components, as evidenced by the aforementioned comparisons and analyses. Further calculating the wavefield energy for the above wavefield snapshot display area and comparing the variations of wave energy in relative changes over time progression and the change at the 8th second with the seismic moment magnitude increasing, as illustrated in Fig. 6. In Fig. 6a, the overall errors in wavefield energy consistently remain below 1 percent as the wave propagates near the source area with small magnitude, signifying that the linear assumption is adequate for the three basic moment tensor sources. In Fig. 6b, the changing curves for the DC source display less smoothness than those for the CLVD, and the relative change in rotational components consistently outweighs this in translational components. Moreover, the curves demonstrate a nearly exponential increase with rising earthquake magnitude. Upon reaching a strong magnitude of 7, especially for the ISO source, the errors in rotational motions reach 25 percent, while these in translation amount to approximately 10 percent. The error due to CLVD sources can also reach about 5 %, while the DC-induced error remains small. Because the DC source component typically dominates the focal mechanisms for the majority of earthquakes, as opposed to the ISO component (Zhao and Zhang, 2022), it can be inferred that the approximation of linear scenario is well-suited for the majority of~~

~~seismic body waves simulations, except in instances of strong seismic activity.~~

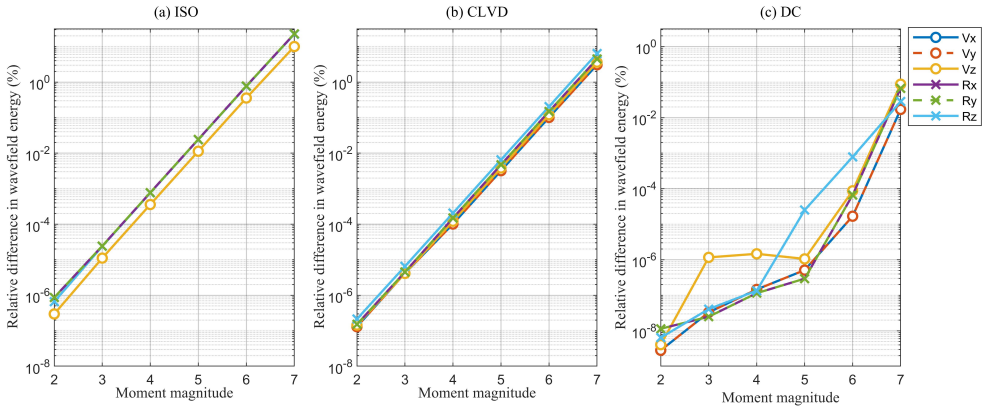

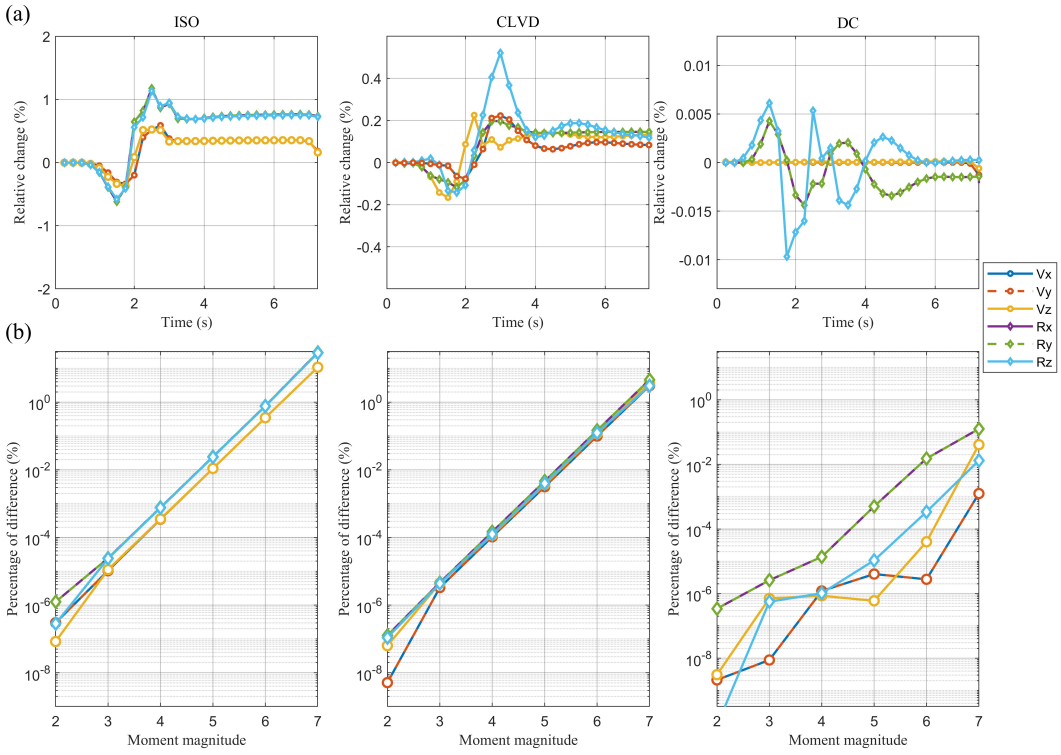

Figure 6. Relative changes ~~of~~ in wavefield energy induced by nonlinearity in the simulations of (a) ISO, (b) CLVD, and (c) DC sources ~~with (a) spreading time~~at 6th second with increasing moment magnitude

Fig. 7 showcases the temporal evolution of wavefield energy between nonlinear and linear models for a magnitude 6 earthquake. Within the first 4 to 6 seconds of seismic wave propagation, intricate phase interactions may result in an overall energy

reduction. Subsequently, wavefield energy difference due to nonlinearity stabilizes, with a more significant energy increase in the rotational component than the translational components. The ISO source model exhibits the most prominent increase in nonlinear relative error with wave propagation, followed by CLVD-type source (Fig. 7b). In the DC source model, nonlinear effects are minimal, with negligible changes induced by nonlinearity in all components except the Rz component (Fig. 7c).

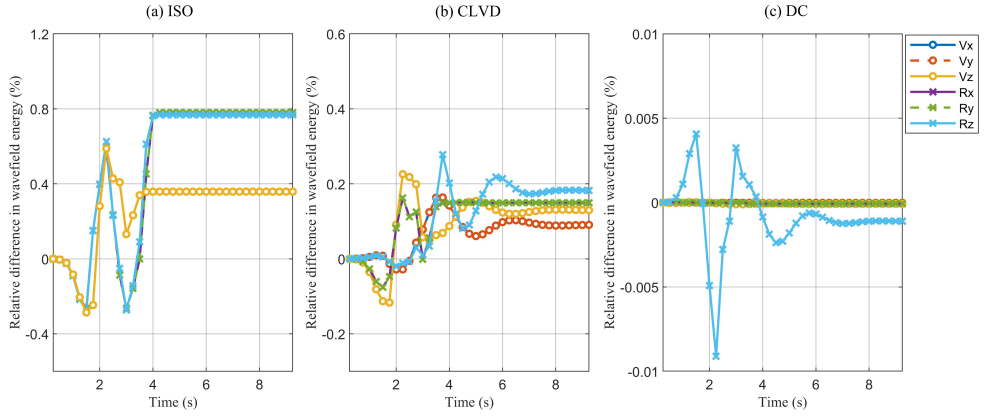

~~and (b) increasing earthquake magnitude~~

Figure 7. Relative changes in wavefield energy induced by nonlinearity in the simulations of (a) ISO, (b) CLVD, and (c) DC sources (Mw6) with increasing time

Based on the preceding results, current seismometers possess sufficient accuracy to capture nonlinearity-induced anomalies in wavefield intensity as demonstrated in simulations. However, it is crucial to observe that these simulations exhibiting prominent anomalies utilize larger magnitude seismic sources and model wave propagation over approximately 30 km, representing near-field results. Under such

480 circumstances, the manifestation of nonlinear effects is anticipated to be significant.

481 In contrast, capturing the nonlinearity on seismic waves in small magnitudes or
482 distant seismicity poses greater challenges. The attenuation and scattering of seismic
483 waves with distance and the relatively lower energy released by smaller magnitudes.
484 Consequently, nonlinear effects may be substantially weakened, heightening the
485 complexity of observation and identification. Thus, given current technological and
486 observational constraints, studying the nonlinear effects of strong earthquakes
487 emerges as a more practical and feasible option.

488 4 ~~Seismic o~~Observations and simulations of two ~~Taiwan~~ earthquakes

489 Two earthquakes along the Taiwan coast are referenced to establish seismic
490 models for simulating wave propagation in both linear and nonlinear media. These
491 simulations aim to preliminarily assess the nonlinear effects of more complex seismic
492 source mechanisms. The spatial difference accuracy in these simulations is set to 10th
493 order.

494 4.1 Hualien earthquakes

495 Taiwan, situated at the ~~confluence~~ juncture of three prominent ~~significant~~ tectonic
496 plates~~, ,~~ the Philippine Sea Plate, the Eurasia Plate, and the Pacific Ocean
497 Plate~~,~~ experiences ~~, experiences~~ frequent ~~seismic activity, particularly~~ moderate to
498 large earthquakes annually ~~annually~~ (Zheng et al., 2005). The 2018 Hualien
499 earthquake ~~(with a magnitude of~~ M_W 5.41 ~~(~~, referred to as E1) and the 2019 Hualien
500 earthquake~~(with a magnitude of~~ M_W 6.13 ~~(~~, referred to as E2)~~,~~ occurred along

Taiwan's eastern coastline, with ~~epicenter depths of 15 km and 30 km~~15-km and 30-km epicenter depths, respectively~~, occurred off the eastern coast of Taiwan~~. The epicenter locations and station configurations, as ~~placements~~ depicted by GMT (Wessel et al., 2019), are shown in Fig. ~~8~~7. To directly observe seismic rotational rates, ~~A b~~BlueSeis-3A fiber-optic rotational seismometers, characterized by a self-noise of up to 2×10^{-8} $rad/s/\sqrt{Hz}$ and a bandwidth of 0.001-100 Hz (Bernauer et al., 2018; Cao et al., 2021) ~~was~~were ~~placed~~deployed at the Nanao ~~the NA01~~ station (NA01) to record E1 ~~station~~ and at the Qingyuanshan station (QS01) to record E2~~in the center of the array to directly record the seismic rotational rates (Bernauer et al. 2018; Cao et al., 2021).The receiver for E2, located in Fujian province, is positioned 327 km from the epicenter (Fig. 7a). Additionally, a seismic array comprising seven 3C translational seismometers was deployed approximately 53 km from the epicenter of E1 (Yuan et al., 2020) (Fig. 7b).~~

According to the information~~monitoring data~~ from the U.S. Geological Survey (USGS, https://www.usgs.gov/), both E1 and E2 were triggered by reverse faulting mechanisms~~faults,. and~~ The focal mechanisms represented by beach balls ~~s representing their focal mechanisms~~ are shown in Fig. 8~~7~~b. The moment tensor parameters of E1 and E2 are detailed ~~presented~~ in Eqs. (2~~0~~) and (3~~1~~), respectively.

519

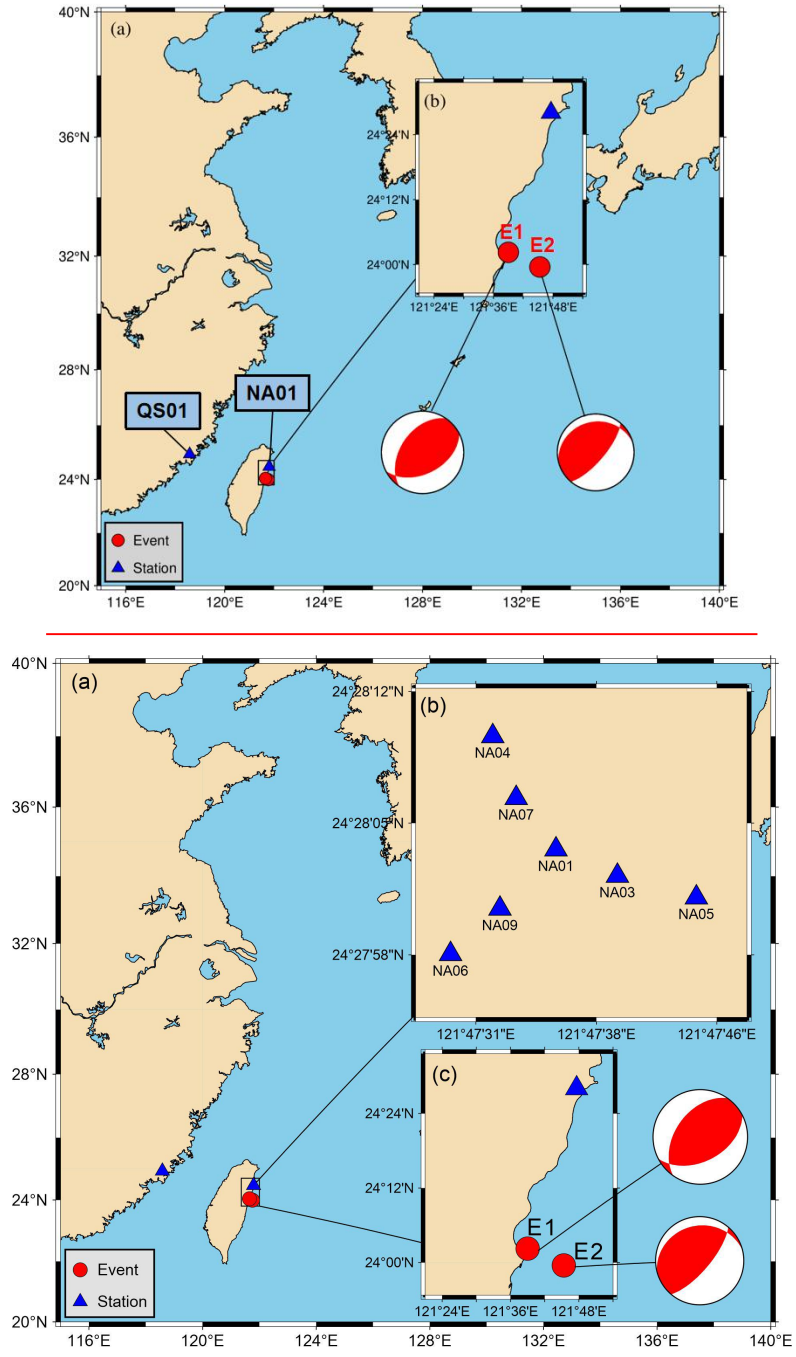

520

521 **Figure 8~~7~~.** Epicenters and observation sites of ~~the two earthquakes~~E1 and E2

522
$$M_{xx} = -7.569\times10^{16}, M_{yy} = -2.373\times10^{16}, M_{zz} = 9.942\times10^{16}$$
$$M_{xz} = 7.372\times10^{16}, M_{yz} = -1.0965\times10^{17}, M_{xy} = 4.156\times10^{16} \quad (22~~0~~)$$

523
$$M_{xx} = -1.064\times10^{18}, M_{yy} = -7.607\times10^{17}, M_{zz} = 1.8247\times10^{18}$$
$$M_{xz} = 3.141\times10^{17}, M_{yz} = 3.155\times10^{17}, M_{xy} = 1.114\times10^{18} \quad (23~~1~~)$$

524

525 4.2 Earthquake simulations ~~of the Taiwan earthquakes~~

To simulate E1 and E2, we implemented free-surface condition at the upper surface and absorbing boundary conditions in other directions of the 3D model. According to the CRUST1.0 model (Laske et al., 2013), the subsurface medium ~~at~~ beneath the observation station of E1 ~~observation station~~ is divided into five distinct layers, as detailed in Table 1. ~~The 3D model is constructed with a size of 60 km (x, NS) × 20 km (y, EW) × 30 km (z, vertical) to suit the specifics of the observation system, with the corresponding parameters shown in Table 2.~~ Given the region's relatively stable geological structure and the focus of the current study is not exploring how medium properties affect the propagation of nonlinear seismic waves, we adopted a simplified strategy by using same stratigraphic parameter settings for simulating the two earthquakes.

Table 1 ~~Underground layered medium~~Physical properties of media ~~at observing stations~~for simulations of E1 and E2

Layer	Thickness (km)	Vp (km/s)	Vs (km/s)	ρ (kg/m³)
1	0.50	2.50	1.07	2.11
2	10.12	5.80	3.40	2.63
3	9.81	6.30	3.62	2.74
4	9.82	6.90	3.94	2.92
5	-	7.70	4.29	3.17

Table 2 Simulation parameters for E1

Items	Parameters
Source type	Eq. (20)
Central frequency	1 Hz
Grid interval	1 km
Time interval	5 ms
Source ~~position~~location	(0, 0, 15 km)
Receiver location~~position~~	(53 km, ~~-~~4 km, 0 km)
Recording time	30 s

To simulating E1, the model size is 60 km (x) × 20 km (y) × 30 km (z) to suit the observation syste. The simulation parameters are shown in Table 2.

.—

Fig. 9a ~~Sorting~~ displays ~~t~~the synthetic records ~~from model 1~~of E1, showcasing ~~at coordinates X=53 km and Y=4 km, corresponding to the NA01 station, the seismic waveforms are presented in Fig. 8a. It can be found that, apart from~~ the direct P- and S-waves, ~~alongside, E1 predominantly exhibits~~ elliptical polarization within the X-Z vertical plane and rotational movements around the Y-axis induced by Rayleigh waves ~~in the north-south vertical plane~~. The large amplitude difference in magnitude ~~order of magnitude difference in amplitude~~ between the ~~theoretical~~ simulations and ~~actual observations~~the observations –can be attributed to~~is due to~~ the ~~assumption~~ difference between the elastic simulation media and actual viscoelastic media, leading to significant energy attenuation in observations~~of elastic media, though the actual propagation media are usually viscoelastic, which will absorb and attenuate seismic energy and highfrequency~~.

~~The unavoidable site effect leads to the practical observation in Fig. 8b displaying significantly stronger horizontal components than vertical ones (Abercrombie, 1997; Guatteri et al., 2001).~~ Fig. 9b shows the complexity of seismic waves after P- and S-wave arrivals in translational components and R_Z components, influenced by ~~The~~ site effect and the nearly northeast strike of the seismogenic fault result in pronounced ~~translational components and R_Z component recordings mixed with complex seismic waves after P- and S-wave arrivals~~,. This indicates~~ing~~ the presence of Love waves and ~~significant~~ deviations ~~disparities between the actual Earth's medium and~~fom the

simplified Crust model. ~~Fig. 8 also shows that~~ Tthe simulated rotational components are significantly ~~1000 times of magnitude~~ weaker (1000 times) than the simulated translational components, ~~but~~ yet the observed rotation~~al motions~~ are only 250 times weaker than the translational ones. This discrepancy may suggest that observed rotation is stronger than the theoretically anticipated. However, multiple factors can affect observed records, and the observed typically exhibit richer high-frequency signals showing stronger rotational energy. So further in-depth analysis and comparison are required before comprehensively identifying and determining the influencing factors.

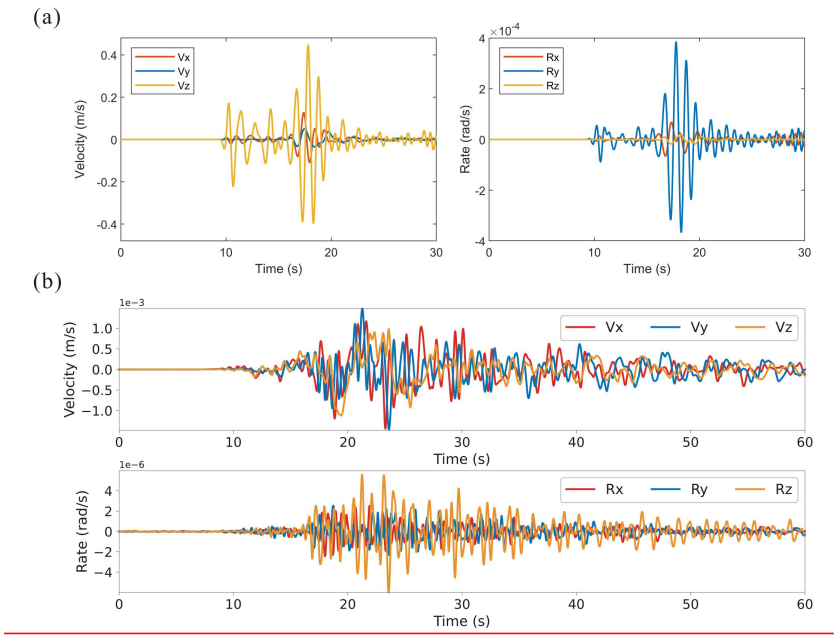

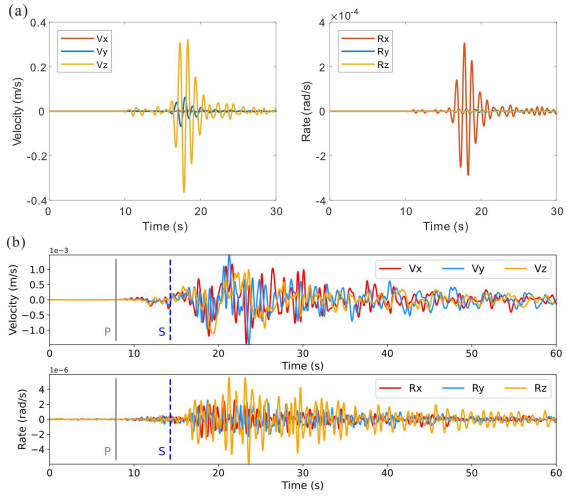

Figure 98. 6C seismic records of (a) ~~theoretical~~ simulation under linear small deformation and (b) actual observation for E1. In (b), ~~for the real seismic records,~~ a band-pass filter of 0.1 Hz to 2 Hz is applied

Fig. 10 presents a comparision of 6C root-mean-square (RMS) amplitude (Fig. 10a) and normalized time-frequency spectrum difference (Fig. 10b) between linear and nonlinear seismic models. RMS amplitudes within a 2-second window were computed at 1-second intervals, with relative change rates derived.

Fig. 10a reveals minor RMS amplitude anomalies attributed to nonlinearity, with the rotational components smaller than the translational components, and translational errors not exceeding 0.1%. For the E1 simulation, linear approximation errors are negligible. In Fig. 10b, the seismic phases affected vary in translational and rotational components. Rotational components exhibit greater impact of nonlinearity on direct S-waves and surface waves, whereas in the translational components, particularly in Vx and Vz, nonlinearity shows heightened effects on p-waves, with the surface waves in the Vy component also affected.

~~, and the corresponding arrival times of P and S waves are calculated according to the iasp91 model (Kennett and Engdahl, 1991)~~

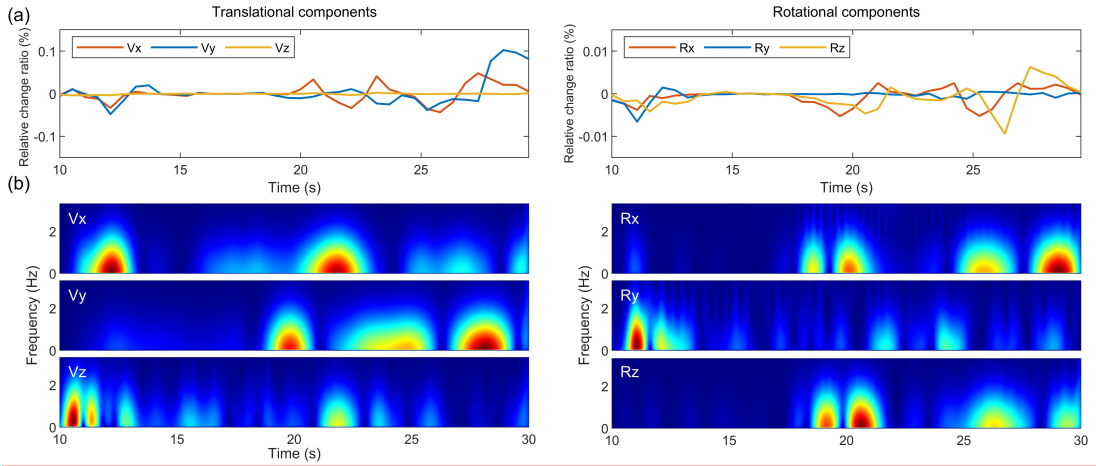

Figure 10. Relative change in RMS amplitude (a) and normalized time-frequency difference (b) of translational components (left subfigures) and rotational components (right subfigures) between linear and nonlinear scenarios

Table 3 Simulation ~~p~~Parameters for ~~simulating model 2 (~~E2~~)~~.

Items	Parameters
Source type	Eq. (21)
Central frequency	0.5 Hz
Grid interval	5 km
Time interval	2 ms
Source ~~position~~location	(0, 310 km, 30 km)
Receiver location~~position~~	~~(:,~~ (100, 0 km, 0 km)
Recording time	~~300~~ 200 s

~~The~~ For simulating E2, the model ~~same modeling approach is adopted to simulate E2, with the parameters of model 2 detailed in Table 3, featuring~~is ~~a size of~~ 150 km (x) ×350 km (y) × 50 km (z~~, vertical~~), and the modeling parameters are detailed in

Table 3. ~~The~~ The synthetic 6C seismic records~~ at X=100 km and Y=0 km, corresponding to the receiver station, are extracted from the simulation result of model 2, as displayed in~~ (Fig. 119a)~~. The simulated records~~ show a dominance of the Vz component over the ~~V_Z over V_X and V_Y~~ Vx and Vy components, ~~with~~ while the ~~R_X~~ Rx and ~~R_{Y}~~Ry components exhibit~~ing~~ greater ~~more~~ strength than the ~~R_Z~~Rz component, ~~showcasing~~ indicating the rotational motions primarily occurring in the horizontal direction. ~~In addition to the direct P and S waves and surface waves, this intense seismic shock generated strong secondary waves.~~ In the actual observed~~ation~~ records (Fig. 119b), where the seismometer~~station~~ is positioned ~~located~~ on a solid rock within a tunnel, indicate a slight dominance of the Vz component ~~is slightly stronger than~~over the Vx and Vy components, while the Rz component is slightly weaker than the Rx and Ry components, which in general aligns with the relative amplitude strength of theoretical simulations. These observations ~~is~~ suggest~~s~~ that the rotational motions for E2 are predominantly ~~in~~ horizontal ~~directions~~, and the ~~the~~ site effect is relatively weaker. ~~In addition, t~~The amplitude difference between the actual observed rotational and translational components is smaller than the amplitude difference between the simulated ~~advective~~ translational and rotational components, ~~and the observed rotational component is relatively stronger,~~ consistent with~~which is the same as~~ the characteristic shown in Fig. 9.~~ That is consistent with previous studies that have argued that the observed rotational components have a relatively stronger amplitude than the rotational component converted from translational components (Teisseyre et al., 2003).~~

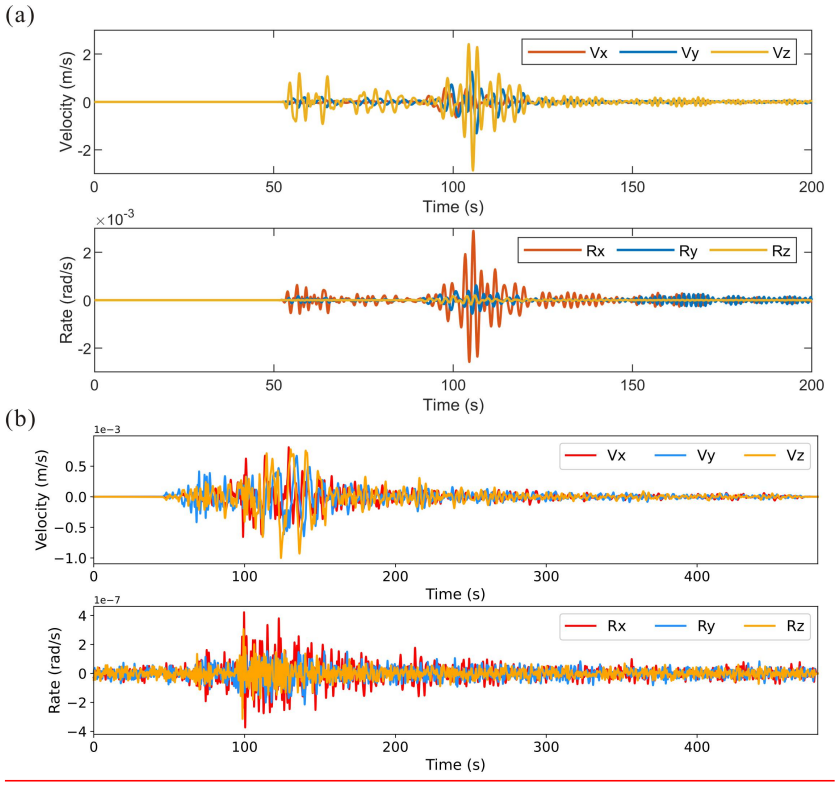

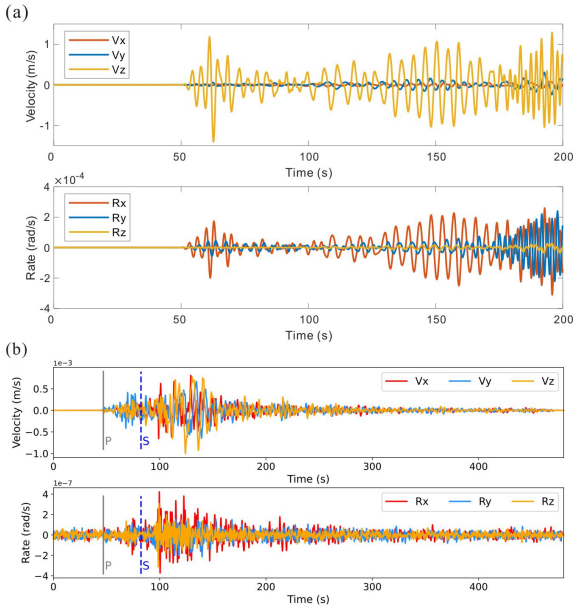

Figure 119. 6C seismic records of (a) ~~theoretical~~ simulation under linear small deformation and (b) actual observation for E2. In (b), ~~for the real seismic records,~~ a band-pass filter of 0.1 Hz to 1 Hz is applied~~, and the corresponding arrival times of P and S waves are calculated according to the iasp91 model (Kennett and Engdahl, 1991)~~

633

634 Fig. 12(a) presents the root mean square (RMS) amplitudes of E2 from linear
635 simulations, with the results incorporating nonlinearity depicted as error bars. It
636 shows that nonlinearity's impact is more significant on the translational components
637 than the rotational motions (generally longer error bars). The Vz component
638 experiences a greater influence (generally wider error bars) among the translational
639 components, and the the Rx-component RMS amplitude is more affected. Fig. 12(b)
640 illustrates that both direct S-waves and surface waves in both translational and
641 rotational components are primarily affected by nonlinearity, albeit with distinct
642 seismic phases affected within their respective frequency spectra. Additionally, the
643 reflected waves on the Vz component also exhibit considerable errors.

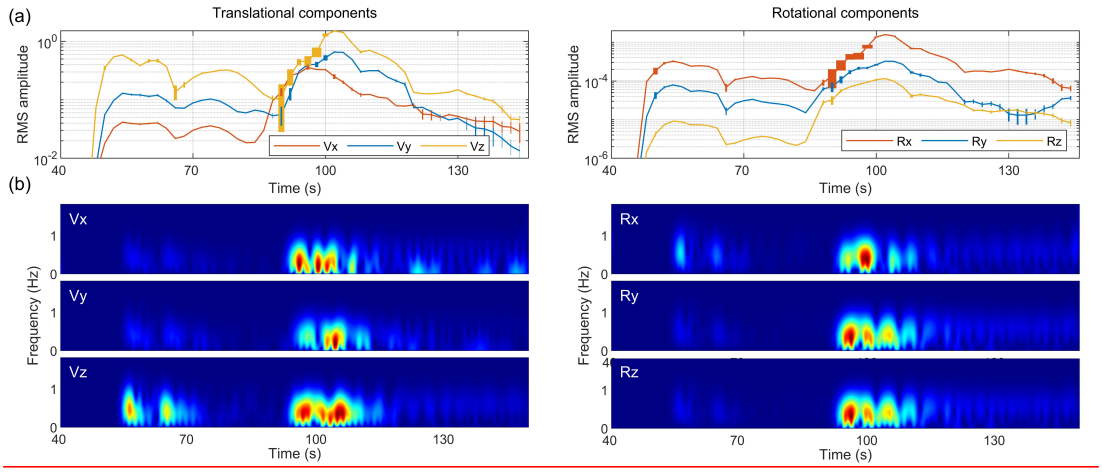

644

645 **Figure 12.** Relative change in RMS amplitude (a) and normalized time-frequency
646 difference (b) of translational components (left subfigures) and rotational components
647 (right subfigures) between linear and nonlinear scenarios

648

649 The simulation results in Section 3 indicate that seismic rotational components are

affected more than translational components due to nonlinearity. However, these comparisons encompass the entire modeled wavefield. Source radiation characteristics may introduce angle-dependent nonlinear effects, potentially impacting translational components more than rotation. This underscores the complexity of nonlinearity and emphasizes the ongoing need for in-depth exploration and research in this area.

~~Following the numerical simulation of E1 and E2 under the conditions of linear and nonlinear simulations, respectively, we make a theoretical comparison by calculating the relative differences between the two scenarios. The relative changes in root-mean-square (RMS) amplitude are used to compare the linear errors of these two earthquakes. The RMS amplitude values of the waveforms recorded in a 2-s time window are calculated at 1-s intervals to reflect the energy of the seismic recordings, and then the relative change percentage of RMS amplitude of the nonlinear simulation results relative to that of the linear simulation is derived accordingly, and the results are shown in Fig. 10.~~

~~In Fig. 10a, it can be seen that the error of the nonlinear simulation of E1 is very small relative to the linear simulation, and only the error on the V_X component is slightly larger but is less than 0.4 %. This indicates that for the simulation of E1, the error introduced by the linear approximation is basically negligible. For the results of E2 in Fig. 10b, the translational components show larger errors than the rotational components, especially the V_X and V_Y components, with errors up to 10 %, and the errors on the V_Z components are basically within 5 %; the linear approximation errors~~

~~on the three rotational components are even smaller, basically within 2 %. For the body waves dominated records before 120 s, R_X and R_Y components reflect a larger error percentage than R_Z component. In the surface-wave records after the 150 s, the R_Z component shows increased nonlinear errors. These results indicate that the linear simplification of rotation for the elastomer strain process has a small error for the rotational component but produces a larger wavefield error on the translational components.~~

~~The linear approximation produces more errors on the translational components obtained from real earthquake simulations, probably because the wavefield energy of rotational component decays faster in natural earthquakes (Lee et al., 2009; Lai and Sun, 2017). Besides, the simulation results of **E**2 show a larger difference between linearity and nonlinearity than that of **E**1, which is about ten times larger, mainly because of the increased source energy of **E**2. So, for weak and moderate earthquakes, the effect of nonlinearity may be negligible, and the linear approximation can meet the research accuracy. It can also be attributed to the fact that the two earthquakes have different source mechanisms, which makes its linear approximation error larger.~~

5 Discussion~~s~~

In contrast to traditional wave propagation limited to linear terms, the Green strain tensor is expressed as a function encompassing both the strain tensor and the rotation tensor. By incorporating nonlinear components , the elastic wave equations now incorporate third-order derivatives of the displacement field. These higher-order

694 nonlinear terms significantly influence the dynamic properties of seismic waves,
695 affecting both volume changes and shear deformation during material deformation.
696 While ISO source simulation in nonlinear media suggests potential coupling
697 between P-waves and S-waves, actual observations reveal more intricate nonlinear
698 effects constrained by multiple factors. Although numerical simulations demonstrate
699 S-wave generation, this finding cannot be generalized to all real-world earthquakes.
700 The existence and intensity of S-waves in natural scenarios necessitate further field
701 observation and theoretical research.
702 Current simulation efforts are preliminary, limited to basic theoretical exploration
703 in idealized homogeneous isotropic elastic media. These models solely focus on three
704 basic moment tensor source types and utilize point source loading. However, natural
705 earthquakes exhibit far greater complexity in source and media characteristics,
706 including diverse fault rupture processes, anisotropic medium properties, site effects
707 and so on. Factors such as seismic source mechanism, propagation path, surface
708 conditions exert complex and unclear influences on nonlinear effects. These factors
709 interact in complex ways, impacting seismic wave propagation.
710 Since the mechanics of seismic rotation may be related to nonlinear elasticity
711 (Guyer and McCall, 1995; Guyer and Johnson, 1999), asymmetric moment tensor
712 (Teisseyre et al., 2003; Teisseyre, 2010), medium heterogeneity, anisotropy (Pham et
713 al., 2010; Sun et al., 2021), and site effects, by examining the intimate relationship
714 between nonlinear effects and propagation path and medium characteristics, we can
715 gain a more objective and accurate understanding of the impact of nonlinearity on

716 seismic waves, particularly regarding rotational components.

717 ~~Compared with the traditional theory of seismic wave propagation in~~
718 ~~homogeneous elastic media, the Green strain tensor is a function of both the strain~~
719 ~~tensor and the rotation tensor, as shown in Eq. (5). Without considering the linear~~
720 ~~approximation of small deformation, the wave propagation equations entail~~
721 ~~three-order differentiations of displacement, with the higher-order terms influenced by~~
722 ~~shear modulus and bulk modulus. Given that earthquakes mostly occur in shallow~~
723 ~~crust or transitional zones between shell and mantle, often considered as planes of~~
724 ~~elastic attributes transformation and stress discontinuity zones, more intricate media~~
725 ~~and focal physics (Olson and Apsel, 1982; Olson and Allen, 2005), such as the model~~
726 ~~featuring a rigid thin-layer sphere (Zhu, 1983), warrant further exploration and~~
727 ~~discussion.~~

728 ~~The mechanics of seismic rotation may be related to various factors, including~~
729 ~~nonlinear elasticity (Guyer and McCall, 1995; Guyer and Johnson, 1999), asymmetric~~
730 ~~moment tensor (Teisseyre et al., 2003; Teisseyre, 2010), medium heterogeneity,~~
731 ~~anisotropy (Pham et al., 2010; Sun et al., 2021), and site effects. This study focuses~~
732 ~~only on isotropic and homogeneous media and three fundamental moment tensor~~
733 ~~sources in the simulations of nonlinear small deformation. Therefore, the effect of~~
734 ~~nonlinear geometric relation on wave propagation, especially for rotational~~
735 ~~components, necessitates further investigation by testing the slipping angle, the shear~~
736 ~~moment, the elastic parameters, and the anisotropy, among others. The current~~
737 ~~discussion concentrates on wave propagation and the characteristics of 6-component~~

~~wavefields excited by three basic moment tensor sources to discuss the theoretical approximation stemming solely from the linear assumption of small deformation, with further analyses of other contributing factors slated for future research endeavors.~~

~~Observations and simulations of Taiwan Hualien earthquakes have verified the existence of rotational motions along the northeast fault, resulting in prominent Rayleigh wave recordings and indicative of a vertical slipping mechanism in the earthquake rupture process. In addition, the observation of stronger $\mathbf{R}_Z$ component and two horizontal components suggests the presence of Love surface waves., signifying clear horizontal slipping and torsion. This finding, aligning with Yu et al.'s (1999) discovery, reveals the existence of horizontal rotational mechanisms within the seismic belt of Taiwan attributed to the Pacific Plate beneath the Eurasian Plate from the east, coupled with northward pressure exerted by the Philippines Sea Plate.~~

~~The simulations show the nonlinear effect cannot be neglected for near, regional, and strong earthquakes, and that the rotational components observed at ground surface will be stronger than the theoretical one, consistent with previous research. Simulations in this study only portray the sources and medium in a simplified way. The simulations of real earthquake scenarios present a much more intricate interplay of source mechanisms and propagation mediums, encompassing long propagation distances, and long time scales. So, the simulations of observed earthquakes, especially for strong earthquakes, the nonlinear attributes through which seismic waves couple with each other amplify the discrepancies arising from the nonlinear assumption.~~

6 Conclusions

Utilizing seismic wave equations that assume linear small deformations as a foundational framework, we have derived elastic-wave formulations incorporating Green strain tensor's nonlinear components. Through numerical simulations and analyses in models of three fundamental seismic moment sources and two Taiwan earthquakes, to study the wavefield disparities between linear and nonlinear scenarios of both translational and rotational motions. The principal findings of our study can be summarized as follows.

(i) When simulating ISO sources in media with nonlinear effects, the interaction between seismic waves leads to the generation of S-waves. For CLVD and DC sources, nonlinear effects cause the intensities of P-waves and S-waves on translational components to trend towards equilibrium, while S-waves exhibit prominence on rotational components.

(ii) The impact of nonlinear media on seismic waves varies depending on the source model. The ISO source model is most significantly affected by nonlinear effects, while the DC source model is relatively less affected. As the source intensity increases, the change in seismic wavefield energy caused by nonlinear media exhibits an exponential growth trend.

(iii) In simulations of pure fundamental seismic sources, the error of linear approximation for rotation is more significant in cases of strong earthquakes, while the nonlinear effects produced by microearthquakes and small earthquakes can be

ignored. The S-waves and surface waves recorded by seismic rotational components have certain significance for studying the impact of nonlinearity on the propagation characteristics of seismic waves.

(iiii) Rayleigh waves dominate the simplified simulations of E1 and E2, but the presence of Love waves in actual observations may be related to site effects or complex propagation media. The linear approximation error of E1 simulation is very small, while the error of E2 simulation is larger, due to differences in their magnitude and potentially the radiation azimuth of the seismic source that leads to inhomogeneous nonlinear effects.

~~Based on seismic wave equations assuming linear small deformation, we have derived elastic-wave equations that incorporate nonlinear part of Green strain tensor. By numerical simulations in a three-dimensional full-space homogeneous medium model using the finite difference method, our study discusses the distinctive characteristics of translational and rotational motions elicited by three fundamental moment tensor sources, shedding light on the wavefield differences between linear and nonlinear assumptions. The following conclusions can be drawn from our study.~~

~~(1) Under the influence of the nonlinear Green tensor, the relative displacement, deformation, and strain of spatial mass element in response to external forces are superimposed with nonlinear second-order terms of strain tensor and rotation tensor, resulting in third-order terms of displacement related to the shear and bulk moduli in the propagation of elastic waves.~~

~~(2) Nonlinearity has a greater effect on ISO and CLVD sources than on DC sources,~~

~~and the effect of nonlinearity on the wavefield energy increases exponentially with increasing magnitude. The nonlinear effect for ISO source primarily impacts S waves. CLVD source generates wavefield difference ranging from 10 % to 20 % in the 45° diagonal direction of P-wave front, similar to the anomalies caused by media anisotropy.~~

~~(3) The errors caused by linearity approximation in rotations are more pronounced in pure basic seismic sources. Strong seismic events render the nonlinear effect unbearable in simulations, underscoring the necessity of considering nonlinear effects. In other cases, the linear approximation meets the accuracy requirements, so the linear approximation can be used for relevant questions. Nonlinear small deformation can be a factor in the rotational motion produced by strong earthquakes.~~

~~(4) The simulation of **E**1 and **E**2 primarily feature Rayleigh waves in vertical translation and horizontal rotation. However, actual observations indicate a prevalent existence of Love waves, potentially attributable to site effects or more complicated focal mechanisms. The stronger-energy **E**2 triggered relatively strong Love waves, so its error caused by the resulting nonlinearity is larger.~~

Author contributions. WL: conceptualization, methodology, investigation, formal analysis, writing - original draft. YW: conceptualization, writing - original draft and revised draft. CC: in vestigation, formal analysis. LS: methodology.

Data and resources. The seismic records of **E**1 are provided by the Institute of Earth

826 Sciences, Academia Sinica, Taiwan, China. The translational records of **E**2 are
827 acquired from the Fujian Earthquake Agency.
828
829 **Competing interests.** The contact author has declared that neither of the authors has
830 any competing interes.
831
832 **Disclaimer.** Publisher's note: Copernicus Publications remains neutral with regard to
833 jurisdictional claims made in the text, published maps, institutional affiliations, or any
834 other geographical representation in this paper.
835
836 **Financial support.** This research is financially supported by the National Natural
837 Science Foundation of China (No. 42150201、No. 62127815、No. U1839208).
838
839 **References**
840 ~~Abercrombie, R. E.: Near-surface attenuation and site effects from comparison of~~
841 ~~surface and deep borehole recordings, Bull. Seismol. Soc. Am., 87 (3),731~744,~~
842 ~~https://doi.org/10.1029/96JB03485, 1997.~~
843 Aki, K., and P. G. Richards. Quantitative seismology, 2nd ed, California: University
844 Science Books, https://doi.org/10.1029/2003EO210008, 2002.
845 Bataille, K., Contreras, M.: Nonlinear elastic effects on permanent deformation due to
846 large earthquakes, Phys. Earth Planet. Inter., 175(1), 47-52,
847 https://doi.org/10.1016/j.pepi.2008.02.016, 2009.
848 Bernauer, F., Wassermann, J., Guattari, F., Frenois, A., Bigueur, A., Gaillot, A., de

Toldi, E., Ponceau, D., Schreiber, U., and Igel, H.: BlueSeis3A: Full characterization of a 3C broadband rotational seismometer, Seismol. Res. Lett., 89(2A), 620–629, https://doi.org/10.1785/0220170143, 2018.

Bernauer, M., Fichtner, A., and Igel, H.: Reducing nonuniqueness in finite source inversion using rotational ground motions, J. Geophys. Res.-Solid Earth, 119(6), 4860-4875, https://doi.org/10.1002/2014JB011042, 2014.

Cao, Y. W., Chen, Y. J., Zhou, T., Yang, C. X., Zhu, L. X., Zhang, D. F., Cao, Y. J., Zeng, W. Y., He, D., and Li, Z. B.: The development of a new IFOG-based 3C rotational seismometer, Sensors, 21(11), 3899, https://doi.org/10.3390/s21113899, 2021.

Chen, Q. J., Yin, J. E., and Yang, Y. S.: Time-frequency characteristic analysis of six-degree-freedom ground motion records, Chinese Quarterly of Mechanics, 35, (3), 499-506, https://link.oversea.cnki.net/doi/10.15959/j.cnki.0254-0053.2014.03.033~~https://doi.org/10.15959/j.cnki.0254-0053.2014.03.033~~, 2014 (in Chinese).

Dong, L. G., and Ma, Z. T.: A staggered-grid high-order difference method of one-order elastic wave equation, Chinese J. Geophys., 43(3), 411-419, 2000 (in Chinese).

Donner, S., Bernauer, M., and Igel, H.: Inversion for seismic moment tensors combining translational and rotational ground motions, Geophys. J. Int., 207(1), 562-570, https://doi.org/10.1093/gji/ggw298, 2016.

Feng, X., Fehler, M., Brown, S., Szabo, T. L., and Burns, D.: Short-period nonlinear viscoelastic memory of rocks revealed by copropagating longitudinal acoustic waves, J. Geophys. Res.-Solid Earth, 123(5), 3993–4006, https://doi.org/10.1029/2017JB015012, 2018.

Graizer, V. M.: Strong motion recordings and residual displacements: what are we actually recording in strong motion seismology? Seismol. Res. Lett., 8(4), 635-639, https://doi.org/10.1785/gssrl.81.4.635, 2010.

Graizer, V. M.: Inertial seismometry methods, Earth Physics, 27(1), 51-61, 1991.

Graves, R. W.: Simulating seismic wave propagation in 3D elastic media using staggered-frid finite differences, Bull. Seismol. Soc. Am., 86(4), 1091-1106, 1996.

Gilbert, F.: Excitation of the normal modes of the Earth by earthquake sources, Geophys. J. R. astr. Soc, 22(2), 223-226, https://doi.org/10.1111/j.1365-246X.1971.tb03593.x, 2010.

Guyer, R. A., and McCall, K. P.: Hysteresis, discrete memory, and nonlinear wave propagation in rock: A new paradigm, Phys. Rev. Lett., 74(17), 3491-3495, https://doi.org/10.1103/physrevlett.74.3491, 1995.

Guyer, R. A., and Johnson, P. A.: Nonlinear mesoscopic elasticity: evidence for a new class of materials, Physics Today, 52(4), 30-36, https://doi.org/10.1063/1.882648, 1999.

Hua, S. B., and Zhang, Y.: Numerical experiments of moment tensor inversion with rotational ground motions, Chinese J. Geophys., 65(1), 197-213,

https://doi.org/10.6038/cjg2022P0668, 2022 (in Chinese).

Huras, L., Zembaty, Z., Bonkowski, P. A., and Bobraet, P.: Quantifying local stiffness loss in beams using rotation rate sensors, Mech. Syst. Signal Proc., 151, 107396, https://doi.org/10.1016/j.ymssp.2020.107396, 2021.

Ichinose, G. A., Ford, S. R., and Mellors, R. J.: Regional moment tensor inversion using rotational observations, J. Geophys. Res.-Solid Earth, 126(2), e2020JB020827, https://doi.org/10.1029/2020JB020827, 2021.

Jia, L., Yan, S. G., Zhang, B. X., and Huang, J.: Research on perturbation method for nonlinear elastic waves, J. Acoust. Soc. Am., 148, EL289–EL294, https://doi.org/10.1121/10.0001980, 2020.

Jost, M. L., and Hermann, R. B.: A students guide to and review of moment tensors, Seism. Res. Lett., 60, 37-57, https://doi.org/10.1785/gssrl.60.2.37, 1989.

~~Kennett, B. L. N., and Engdahl, E. R.: Traveltimes for global earthquake location and phase identification, Geophys. J. Int., 105(2), 429–465, https://doi.org/10.1111/j.1365-246X.1991.tb06724.x, 1991.~~

Knopoff, L., and Randall M. J.: The compensated linear-vector dipole: A possible mechanism for deep earthquakes, J. Geophy. Res., 75(26), 4957–4963, https://doi.org/10.1029/JB075i026p04957, 1970.

Kozak, J. T.: Tutorial on earthquake rotational effects: historical examples, Bull. Seismol. Soc. Am., 99(2B), 998-1010, https://doi.org/10.1785/0120080308, 2009.

Lai, X. L., and Sun, Y.: Three component rotational ground motion obtained from

explosive source data, Earth science, 42(4), 645－651, 2017 (in Chinese).

Laske, G., Masters, G., Ma, Z. T., and Pasyanos, M.: Update on CRUST1. 0-A 1-degree global model of ~~Earth's~~ Earth's crust, EGU General Assembly 2013, 15, EGU2013-2658, 2013.

~~Lee, K. H. W., Igel, H., and Trifunac, D. M.: Recent Advances in Rotational Seismology, Seismol. Res. Lett., 80(3), 479-489, https://doi.org/10.1785/GSSRL.80.3.479, 2009.~~Lee, C. E. B., Celebi, M., Todorovska, M. I., and Diggles, M. F.: Rotational seismology and engineering applications — Proceedings for the First International Workshop, Menlo Park, California, U.S.A.—September 18 to 19, 2007: U.S. Geological Survey Open-File Report 2007-1144, 46 p. http://pubs.usgs.gov/of/2007/1144/, 2007.

Li, H. N.: Study on rotational components of ground motion, Journal of Shenyang Architectural and Civil Engineering Institute, 7(1), 88-93, 1991 (in Chinese).

Li, H. N., and Sun, L. Y.: Rotational components of earthquake ground motions derived from surface waves, Earthq. Eng. Eng. Vib., 21(1), 15-23, https://link.oversea.cnki.net/doi/10.13197/j.eeev.2001.01.003,~~https://doi.org/10.13197/j.eeev.2001.01.003,~~ 2001 (in Chinese).

Madariaga, R.: Dynamics of an expanding circular fault, Bull. Seismol. Soc. Am., 66(3), 639-666, https://doi.org/10.1007/BF02246368, 1976.

McCall, K. R.: Theoretical study of nonlinear elastic wave propagation, J. Geophys. Res., 99(B2), 2591-2600, https://doi.org/10.1029/93JB02974, 1994.

Oliveira, C. S., and Bolt, B. A.: Rotational components of surface strong ground motion~~.~~, Earthq. Eng. Struct. D. 18(4), 517–526, https://doi.org/10.1002/eqe.4290180406, 1989.

~~Olson, A. H., and Apsel, R. J.: Finite faults and inverse theory with applications to the 1979 Imperial Valley earthquake, Bull. Seismol. Soc. Am., 72(6A), 1969-2001, https://doi.org/10.1785/BSSA07206A1969, 1982.~~

~~Olson, E. L., and Allen, R. M.: The deterministic nature of earthquake rupture, Nature, 438(7065), 212-215, https://doi.org/10.1038/nature04214, 2005.~~

Pei, Z. L.: Numerical simulation of elastic wave equation in 3-D anisotropic media with staggered-grid high-order difference method, Geophysical Prospecting for Petroleum, 44(4), 308-315, https://doi.org/10.3969/j.issn.1000-1441.2005.04.002, 2005 (in Chinese).

Pham, N. D., Igel, H., Puente, J. D. L., Käser, M., and Schoenberg, M. A.: Rotational motions in homogeneous anisotropic elastic media, Geophysics 75(55), D47-D56, https://doi.org/10.1190/1.3479489, 2010.

Renaud, G., Le Bas, P. Y., and Johnson, P. A.: Revealing highly complex elastic nonlinear (anelastic) behavior of Earth materials applying a new probe: Dynamic acoustoelastic testing, J, Geophys. Res.-Solid Earth, 117, B06202, , https://doi.org/10.1029/2011JB009127, 2012.

Renaud, G., Rivière, J., Le Bas, P. Y., and Johnson, P. A.: Hysteretic nonlinear elasticity of Berea sandstone at low-vibrational strain revealed by dynamic

acoustoelastic testing, Geophys. Res. Lett., 40(4), 715-719, https://doi.org/10.1002/grl.50150, 2013.

Sun, L., Yu, Y., Lin, J. Q., and Liu, J. L.: Study on seismic rotation effect of simply supported skew girder bridge, Earthquake Engineering and Engineering Dynamics, 37(4), 121-128, https://doi.org/10.13197/j.eeev.2017.04.121.sunl.014, 2017 (in Chinese).

Sun, L. X., Wang, Y., Li, W., and Wei, Y. X.: The characteristics of seismic rotations in VTI medium, Appl. Sci.-Basel, 11(22), 10845, https://doi.org/10.3390/app112210845, 2021.

Sun, L. X., Zhang, Z., and Wang, Y.: Six-component elastic-wave simulation and analysis, EGU General Assembly 2018, Geophysical Research Abstracts, 20, EGU2018-14930-1, 2018.

Teisseyre, R., Suchcicki, J., Teisseyre, K. P., Wiszniowski J., and Palangio, P.: Seismic rotation waves: Basic elements of the theory and recordings, Annals of Geophysics, 46(4), 671–685, https://doi.org/10.4401/ag-4375, 2003.

Teisseyre, R.: Tutorial on new developments in the physics of rotational motions, Translated World Seismology, 99(2A), 1028-1039, https://doi.org/10.1785/0120080089, 2010.

TenCate, J. A., Malcolm, A. E., Feng, X., and Fehler, M. C.: The effect of crack orientation on the nonlinear interaction of a P wave with an S wave, Geophys. Res. Lett., 43(12), 6146-6152, https://doi.org/10.1002/2016GL069219, 2016.

Wang, L., Luo, Y. H., and Xu, Y. H.: Numerical investigation of Rayleigh-wave propagation on topography surface, J. Appl. Geophys., 86, 88–97,

https://doi.org/10.1016/j.jappgeo.2012.08.001, 2012.

Wang, X. S., and Lv, J.: The holistic clockwise rotation possibly existed in Taiwan region - in addition on the seismicity feature and earthquake prediction in its adjacent areas, South China Journal of Seismology, 2, 48-54, https://doi.org/10.3969/j.issn.1001-8662.2006.02.008, 2006 (in Chinese).

Wessel, P., Luis, J. F., Uieda, L., Scharroo, R., Wobbe, F., Smith, W. H. F., and Tian, D.: The generic mapping tools version 6, Geochemistry, Geophysics, Geosystems, 20, 5556–5564, https://doi.org/10.1029/2019GC008515, 2019.

Xu, Y. X., Xia, J. H., and Miller, R. D.: Numerical investigation of implementation of airearth boundary by acoustic-elastic boundary approach, Geophysics, 72 (5), SM147–SM153, https://doi.org/10.1190/1.2753831, 2007.

Yan, Y. Y.: Seismic response analysis of high-rise building under different types of multi-dimensional earthquake ground motions (Ph.D. dissertation), Jiangsu University, 2017(in Chinese).

Yu, S. B., Kuo, L. C., and Punongbayan, R. S., Emmanuel, G.R.: GPS observation of crustal deformation in Taiwan-Luzon region, Geophys. Res. Lett., 26(7), 923-926, https://doi.org/10.1029/1999GL900148, 1999.

~~Yuan, S. H., Simonelli, A., Lin, C. J., Bernauer, F., Donner, S., Braun, T., Wassermann, J., and Igel, H.: Six-degree-of-freedom broadband ground-motion observations with portable sensors: Validation, local earthquakes, and signal processing, Bull. Seismol. Soc. Am., 110(3), 953–969, https://doi.org/10.1785/0120190277, 2020.~~

Yang, D.H., Liu, E., Zhang, Z.J., and Teng, J.: Finite-difference modelling in

two-dimensional anisotropic media using a flux-corrected transport technique, Geophys. J. Int., 148(2), 320–328, https://doi.org/10.1046/j.0956-540x.2001.01575.x, 2002.

Zhao, K. C., and Zhang, X. B.: Distinguishing underground nuclear test by matrix decomposition, Acta Scientiarum Naturalium Universitatis Pekinensis, 58(4), 609-614, https://link.oversea.cnki.net/doi/10.13209/j.0479-8023.2022.042~~https://doi.org/10.13209/j.0479-8023.2022.042~~, 2022 (in Chinese).

Zheng, H. S., Z. J. Zhang, and Liu, E. R.: Nonlinear seismic wave propagation in anisotropic media using the flux-corrected transport technique, Geophys. J. Int., 165(3), 943-956, https://doi.org/10.1111/j.1365-246X.2006.02966.x, 2006.

Zheng, X.,F., Cheng, Z.,H., and Zhang, C. H.: The development of seismic monitoring in Taiwan, Seismological and Geomagnetic Observation and Research, 26(3), 100-107, https://doi.org/10.3969/j.issn.1003-3246.2005.03.017, 2005 (in Chinese).

Zhou, C., Zeng, X. Z., Wang, Q. L., and Liu, W. Y., and Wang, C. Z.: Rotational motions of the Ms7.0 Jiuzhaigou earthquake with ground tilt data, Science China Earth Science, 62(5), 832-842, https://doi.org/10.1007/s11430-018-9320-3, 2019.

~~Zhu, Z. X.: On the nonlinear strain measures, Advances in Mechanics, 13(2), 259-272, 1983 (in Chinese).~~